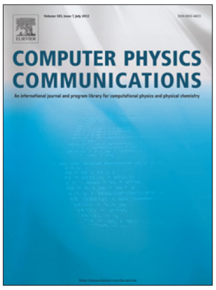

MITHRA 1.0: A full-wave simulation tool for free electron lasers

Arya Fallahi, Alireza Yahaghi, Franz X. Kärtner

PII: S0010-4655(18)30083-3
DOI: https://doi.org/10.1016/j.cpc.2018.03.011
Reference: COMPHY 6456

To appear in: *Computer Physics Communications*

Received date : 2 January 2017
Revised date : 19 February 2018
Accepted date : 8 March 2018

Please cite this article as: A. Fallahi, A. Yahaghi, F.X. Kärtner, MITHRA 1.0: A full-wave simulation tool for free electron lasers, *Computer Physics Communications* (2018), https://doi.org/10.1016/j.cpc.2018.03.011

MITHRA 1.0: A Full-wave Simulation Tool for Free Electron Lasers

Arya Fallahi[a,*], Alireza Yahaghi[a], Franz X. Kärtner[a,b]

[a]*Center for Free Electron Laser Science, DESY, Notkestrasse 85, 22607 Hamburg, Germany*
[b]*Department of Physics, University of Hamburg, Notkestrasse 85, 22607 Hamburg, Germany*

Abstract

Free Electron Lasers (FELs) are a solution for providing intense, coherent and bright radiation in the hard X-ray regime. Due to the low wall-plug efficiency of FEL facilities, it is crucial and additionally very useful to develop complete and accurate simulation tools for better optimizing a FEL interaction. The highly sophisticated dynamics involved in a FEL process was the main obstacle hindering the development of general simulation tools for this problem. We present a numerical algorithm based on *finite difference time domain/Particle in cell* (FDTD/PIC) in a Lorentz boosted coordinate system which is able to fulfil a full-wave simulation of a FEL process. The developed software offers a suitable tool for the analysis of FEL interactions without considering any of the usual approximations. A coordinate transformation to bunch rest frame makes the very different length scales of *bunch size*, *optical wavelengths* and the *undulator period* transform to values with the same order. Consequently, FDTD/PIC simulations in conjunction with efficient parallelization techniques make the full-wave simulation feasible using the available computational resources. Several examples of free electron lasers are analyzed using the developed software, the results are benchmarked based on standard FEL codes and discussed in detail.

Keywords: Free Electron Laser, Finite Difference Time Domain, Particle in Cell, Undulator radiation, Inverse Compton Scattering.
2010 MSC: 00-01, 99-00

PROGRAM SUMMARY

Program Title: MITHRA
Program Files doi: `http://dx.doi.org/10.17632/9f5k4zbtxg.1`
Licensing provisions: GNU General Public License 3
Programming language: C++
Nature of problem: Full-wave simulation of the free electron laser radiation is accomplished by the code. MITHRA transforms the particle positions and momenta to the bunch rest frame using the Lorentz transformation. Electrons entering the undulator start radiating due to the induced wiggling motion. The back-effect of the radiation on the bunch results in the modulation of the electron position, which in turn generates a coherent radiation. This process as the main principle behind the operation of free electron lasers is simulated using Maxwell equations, electron motion equations and relativity principles.
Solution method: Non-standard Finite Difference Time Domain (NSFDTD) combined with Particle-in-Cell (PIC) is implemented in the Lorentz-boosted framework to calculate the FEL radiation. Parallelization is done using both multi-threading (open-MP) and message passing interface (MPI) to maximize the computation efficiency.

1. Introduction

Free Electron Lasers (FELs) are currently serving as promising and viable solutions for the generation of electromagnetic radiation in the whole frequency spectrum ranging from microwaves to hard X-rays [1, 2, 3]. Particularly, in portions of spectrum where common solutions like lasers and other electronic sources do not offer efficient schemes, FEL based devices attract considerable attention and interest. For example, soft and hard X-ray as well as THz frequency ranges are parts of the spectrum where FEL sources are widely used. Recently, coherent X-ray beams have shown unprecedented promises in enabling biologists, chemists and material scientists to study various evolutions and interactions with nanometer and sub-nanometer resolutions [4].

---

[*] Corresponding author
E-mail address: arya.fallahi@cfel.de

Owing to the desire of hard X-ray FEL machines for electrons with ultrarelativistic energies (0.5-1 GeV), these sources are usually giant research facilities with high operation costs and energy consumption. Therefore, it is crucial and additionally very useful to develop sophisticated simulation tools, which are able to capture the important features in a FEL radiation process. Such tools will be very helpful for designing and optimizing a complete FEL facility and additionally useful for detailed investigation of important effects. The last decade had witnessed extensive research efforts aiming to develop such simulation tools. As a result, various softwares like Genesis 1.3 [5], MEDUSA [6], TDA3D [7, 8], GINGER [9], PERSEO [10], EURA [11], RON [12], FAST [13], CHIMERA (previously PlaRes) [14] and PUFFIN [15] are developed and introduced to the community. However, all the currently existing simulation softwares are usually written to tackle special cases and therefore particular assumptions or approximations have been considered in their development [16]. Some of the common approximations in FEL simulation are tabulated in Table 1.

The main goal in the presented research is the analysis of the FEL interaction without considering any of the above approximation. The tool could be used for testing the validity of various approximations in different operation regimes and also a reliable approach for preparing the final design of a FEL facility.

Besides the wide investigations and studies on the conventional X-ray FELs, recently research efforts have been devoted to building compact X-ray FELs, where novel schemes for generating X-ray radiations in a so-called table-top setup are examined and assessed. Various research topics such as laser-plasma wake-field acceleration (LPWA) [17, 18, 19], laser plasma accelerators (LPA) [20, 21], laser dielectric acceleration (LDA) [22] and THz acceleration [23, 24], pursue the development of compact accelerators capable of delivering the desired electron bunches to FEL undulators. Besides such attempts, one promising approach to make a compact undulator is using optical undulators, where the oscillations in an electromagnetic wave realize the wiggling motion of the electrons [25]. Many of the approximations in Table 1, which sound reasonable for static undulators are not applicable for studying an optical undulator radiation. In this regime, due to the various involved length-scales and remarkable impact of the parameter tolerances, having access to a rigorous and robust FEL simulation tool is essential.

One of the difficulties in the X-ray FEL simulation stems from the involvement of dramatically multidimensional electromagnetic effects. Some of the nominal numbers in a typical FEL simulation are:

- Size of the bunch: $\sim 100\,\mathrm{fs}$ or $300\,\mu\mathrm{m}$
- Undulator period: $\sim 1\,\mathrm{cm}$
- Undulator length: $\sim 10-500\,\mathrm{m}$
- Radiation wavelength: $\sim 1-100\,\mathrm{nm}$

Comparing the typical undulator lengths with radiation wavelengths immediately communicates the extremely large space for the values. This in turn predicts very high computation costs to resolve all the physical phenomena, which is not practical even with the existing supercomputer technology. In order to overcome this problem, we exploit Lorentz boosted coordinate system and implement Finite Difference Time Domain (FDTD) [26] method combined with Particle in Cell (PIC) simulation in the electron rest frame. This coordinate transformation makes the bunch size and optical wavelengths longer and shortens the undulator period. Interestingly, these very different length scales transform to values with the same order after the coordinate transformation. Consequently, the length of the computation domain is reduced to slightly more than the bunch length making the full-wave simulation numerically feasible. We comment that the simulation of particle interaction with an electromagnetic wave in a Lorentz boosted framework is not a new concept. The advantage of this technique for the study of relativistic interactions is widely discussed [27, 28]. The method is currently the standard technique for the simulation of plasma-wakefield acceleration [29, 30, 31]. Using Lorentz-boosted equations to solve for FEL physics was previously presented in [32], where the code Warp is adapted to simulate a FEL with static undulator. In [33], the dynamics of a FEL based on optical-lattice undulator is described in the electron rest frame. Here, we are presenting a software dedicated to the analysis of FEL mechanism by solving principal equations in bunch rest frame.

Along with all the benefits offered by numerical simulation in the Lorentz-boosted framework, there exists a disadvantage emanated from treating quantities different from real three-dimensional fields in the laboratory frame. For instance, the field profile along the undulator axis at a certain time does not represent the real radiated field profile, because the fields at various points map to the corresponding values at different time points in the laboratory frame. While this feature introduces difficulties in interpreting and investigating the numerical outputs, as discussed in [27] analysis in the moving frame leads to a considerable computational gain motivating

Table 1: Common approximations in modelling free electron laser radiation

code name	approximation					
	steady state approximation	wiggler-average electron motion	slow wave approximation	forward wave	no space-charge	slice
GENESIS 1.3	optional	✓	✓	✓	—	optional
MEDUSA	optional	—	✓	✓	—	✓
TDA3D	✓	✓	✓	✓	—	no time-domain
GINGER	—	✓	✓	✓	—	—
PERSEO	—	—	—	✓	✓	—
CHIMERA	—	—	—	✓	—	—
EURA	—	✓	✓	✓	—	—
FAST	—	✓	✓	—	—	✓
PUFFIN	—	—	—	✓	✓	—

the FEL analysis in Lorentz-boosted framework. In addition, separate modules and functions can be developed to extract the required plots in stationary frame from the computed values. This approach is implemented in the code MITHRA to obtain the radiated power.

The presented study shows how one can numerically simulate a complete FEL interaction using merely Maxwell equations, equation of motion for a charged particle, and the relativity principles, without specific approximations. In section 2, the whole computational aspects of the numerical method, including the Finite Difference Time Domain (FDTD), Particle In Cell (PIC), current deposition, Lorentz boosting, quantity initialization, and parallelization, are described in detail. In section 3, different examples of free electron lasers are analyzed and the results are presented in conjunction with some discussions.

2. Numerical Implementation

In this section, we present the detailed formalism of Finite Difference Time Domain - Particle In Cell (FDTD/PIC) method in the Lorentz boosted coordinate system. There are many small still very important considerations in order to obtain reliable results, which converge to the real values. For example, the method for electron bunch generation, particle pusher algorithm and computational mesh truncation need particular attention.

2.1. Finite Difference Time Domain (FDTD)

FDTD is perhaps the first choice coming to mind for solving partial differential equations governing the dynamics of a system. Despite its simple formulation and second order accuracy, there are certain features in this method like explicit time update and zero DC fields, which makes this method a superior choice compared to other algorithms [26]. FDTD samples the field in space and time at discrete sampling points and represents the partial derivatives with their discrete counterparts. Subsequently, update equations are derived based on the governing differential equation. Using these updating equations, a time marching algorithm is acquired which evaluates the unknown functions in the whole computational domain throughout the simulation time. In the following, we start with the wave equation which is the governing partial differential equation for our electromagnetic problem.

2.1.1. Potential Equation

The physics of electromagnetic wave and its interaction with charged particles in free space is mathematically formulated through the well-known Maxwell's equations:

$$\nabla \times \boldsymbol{E} = -\frac{\partial \boldsymbol{B}}{\partial t} \tag{1}$$

$$\nabla \times \boldsymbol{B} = \mu_0 \boldsymbol{J} + \mu_0 \varepsilon_0 \frac{\partial \boldsymbol{E}}{\partial t} \tag{2}$$

$$\nabla \cdot \boldsymbol{E} = -\frac{\rho}{\varepsilon_0} \tag{3}$$

$$\nabla \cdot \boldsymbol{B} = 0 \tag{4}$$

These equations in conjunction with the electric current equation $\boldsymbol{J} = \rho \boldsymbol{v}$ ($\boldsymbol{v}$ is the charge velocity) and the Lorentz force equation:

$$\boldsymbol{F} = q(\boldsymbol{E} + \boldsymbol{v} \times \boldsymbol{B}) \tag{5}$$

are sufficient to describe wave-electron interaction in free space. Moving free electrons introduce electric current which enters into the Maxwell's equations as the source. Electric and magnetic fields derived from these equations are subsequently employed in the Lorentz force equation to determine the forces on the electrons, which in turn determine their motions. As it is evident from the above equations, there are two unknown vectors ($\boldsymbol{E}$ and $\boldsymbol{B}$) to be evaluated, meaning that six unknown components should be extracted from the equations. However, since these two vectors are interrelated and specially because there is no magnetic monopole in the nature ($\nabla \cdot \boldsymbol{B} = 0$), one can recast Maxwell's equations in a wave equation for the magnetic vector potential ($\boldsymbol{A}$) and a wave equation for the scalar electric potential (φ):

$$\boldsymbol{\nabla}^2 \boldsymbol{A} - \frac{1}{c^2}\frac{\partial^2}{\partial t^2}\boldsymbol{A} = -\mu_0 \boldsymbol{J} \tag{6}$$

$$\nabla^2 \varphi - \frac{1}{c^2}\frac{\partial^2 \varphi}{\partial t^2} = -\frac{\rho}{\varepsilon_0} \tag{7}$$

where $c = 1/\sqrt{\mu_0 \varepsilon_0}$ is the light velocity in vacuum. In the derivation of above equations, the Lorentz gauge $\nabla \cdot \boldsymbol{A} = -\frac{1}{c^2}\frac{\partial \varphi}{\partial t}$ is used. The original $\boldsymbol{E}$ and $\boldsymbol{B}$ vectors can be obtained from $\boldsymbol{A}$ and φ as:

$$\boldsymbol{B} = \nabla \times \boldsymbol{A} \tag{8}$$

$$\boldsymbol{E} = -\frac{\partial \boldsymbol{A}}{\partial t} - \nabla \varphi \tag{9}$$

In addition to the above equations, the charge conservation law written as

$$\nabla \cdot \boldsymbol{J} + \frac{\partial \rho}{\partial t} = 0, \tag{10}$$

should not be violated in the employed computational algorithm. This is the main motivation for seeking proper current deposition algorithms in the FDTD/PIC methods used for plasma simulations. It is immediately observed that the equations (6), (7), (10) and the Lorentz gauge introduce an overdetermined system of equations. In other words, once a current deposition is implemented that automatically satisfies the charge conservation law, the Lorentz gauge will also hold, provided that the scalar electric potential (φ) is obtained from (7). However, due to the space-time discretization and the interpolation of quantities to the grids, a suitable algorithm that holds the charge conservation without violating energy and momentum conservation does not exist. The approach that we follow in MITHRA is using the discretized form of (6) and (7) with the currents and charges of electrons (i.e. macro-particles) as the source and solving for the vector and scalar potential. It was shown by Umeda et al. [34], that by using similar weighting functions for both current density ($\boldsymbol{J}$) and charge density (ρ), and a proper discretization of current density based on positions of the macro-particles according to a Zigzag scheme, a charge conserving deposition scheme can be obtained. Here, we have implemented the Zigzag scheme to maintain the charge conservation in MITHRA. To obtain the fields $\boldsymbol{E}$ and $\boldsymbol{B}$ at the grid points, we use the momentum conserving interpolation, which will be explained in the upcoming sections.

2.1.2. *FDTD for Wave Equation*

In cartesian coordinates, a vector wave equation is written in form of three uncoupled scalar wave equations. Therefore, it is sufficient to apply our discretization scheme only on a typical scalar wave equation: $\nabla^2\psi - \frac{1}{c^2}\frac{\partial^2 \psi}{\partial t^2} = \zeta$, where ψ stands for A_l ($l \in \{x, y, z\}$); and ζ represents the term $-\mu_0 J_l$. Let us begin with the central-difference discretization scheme for various partial differential terms of the scalar wave equation at the point $(i\Delta x, j\Delta y, k\Delta z, n\Delta t)$. In the following equations, $\psi^n_{i,j,k}$ denotes the value of the quantity ψ at the point $(i\Delta x, j\Delta y, k\Delta z)$ and time $n\Delta t$. The derivatives are written as follows:

$$\frac{\partial^2}{\partial x^2}\psi(x,y,z,t) \simeq \frac{\psi^n_{i+1,j,k} - 2\psi^n_{i,j,k} + \psi^n_{i-1,j,k}}{(\Delta x)^2} \tag{11}$$

$$\frac{\partial^2}{\partial y^2}\psi(x,y,z,t) \simeq \frac{\psi^n_{i,j+1,k} - 2\psi^n_{i,j,k} + \psi^n_{i,j-1,k}}{(\Delta y)^2} \tag{12}$$

$$\frac{\partial^2}{\partial z^2}\psi(x,y,z,t) \simeq \frac{\psi^n_{i,j,k+1} - 2\psi^n_{i,j,k} + \psi^n_{i,j,k-1}}{(\Delta z)^2} \tag{13}$$

$$\frac{\partial^2}{\partial t^2}\psi(x,y,z,t) \simeq \frac{\psi^{n+1}_{i,j,k} - 2\psi^n_{i,j,k} + \psi^{n-1}_{i,j,k}}{(\Delta t)^2}. \tag{14}$$

Combining these four equations, one obtains the value of ψ at instant $(n+1)\Delta t$ in terms of its value at $n\Delta t$ and $(n-1)\Delta t$:

$$\begin{aligned}\psi^{n+1}_{i,j,k} = &-\psi^{n-1}_{i,j,k} + \alpha_1\psi^n_{i,j,k} + \alpha_2\psi^n_{i+1,j,k} + \alpha_3\psi^n_{i-1,j,k}\\ &+ \alpha_4\psi^n_{i,j+1,k} + \alpha_5\psi^n_{i,j-1,k} + \alpha_6\psi^n_{i,j,k+1} + \alpha_7\psi^n_{i,j,k-1}\\ &+ \alpha_8\zeta^n_{i,j,k}\end{aligned}$$

where the coefficients $\alpha_1, \ldots, \alpha_7$ are obtained from:

$$\alpha_1 = 2\left[1 - \left(\frac{c\Delta t}{\Delta x}\right)^2 - \left(\frac{c\Delta t}{\Delta y}\right)^2 - \left(\frac{c\Delta t}{\Delta z}\right)^2\right],$$

$$\alpha_2 = \alpha_3 = \left(\frac{c\Delta t}{\Delta x}\right)^2, \qquad \alpha_4 = \alpha_5 = \left(\frac{c\Delta t}{\Delta y}\right)^2, \tag{15}$$

$$\alpha_6 = \alpha_7 = \left(\frac{c\Delta t}{\Delta z}\right)^2, \qquad \alpha_8 = (c\Delta t)^2 .$$

The term $\zeta^n_{i,j,k}$ is the magnitude of the source term at the time $n\Delta t$, which is calculated from the particle motions. Usually, one needs a finer temporal discretization for updating the equation of motion compared to electromagnetic field equations. If the equation of motion is discretized and updated with $\Delta t_b = \Delta t/N$ time steps, the term $\zeta^n_{i,j,k}$ will be written in terms of the value after each N update:

$$\zeta^n_{i,j,k} = -\mu_0 J_l(n\Delta t) = -\mu_0 \rho(n\Delta t) \frac{\boldsymbol{r}^{n+1/2} - \boldsymbol{r}^{n-1/2}}{\Delta t}. \tag{16}$$

As observed in the above equation, the position of particles are sampled at each $n + 1/2$ time step, which later should be considered for updating the scalar potential. This assumption also results in the calculation of charge density at $n + 1/2$ time steps, which should be averaged for obtaining $\rho(n\Delta t)$.

2.1.3. Numerical Dispersion in FDTD

It is well-known that the FDTD formulation for discretizing the wave equation suffers from the so-called numerical dispersion. More accurately, the applied discretization leads to the phase velocity of wave propagation calculated different from (lower than) the vacuum speed of light. This may impact the FEL simulation results particularly during the saturation regime, owing to the important role played by the relative phase of electrons with respect to the radiated light. Therefore, careful scrutiny of this effect and minimizing its impact is essential for the goal pursued by MITHRA.

To derive the equation governing such a dispersion, we assume a plane wave function for $\psi(x, y, z, t)$ as:

$$\psi(x, y, z, t) = e^{-j(k_x x + k_y y + k_z z - \omega t)} \tag{17}$$

in the discretized wave equation. After some mathematical operations, the following equation is obtained for the dispersion properties of central-difference scheme:

$$\frac{\sin^2\left(\frac{k_x\Delta x}{2}\right)}{(\Delta x)^2} + \frac{\sin^2\left(\frac{k_y\Delta y}{2}\right)}{(\Delta y)^2} + \frac{\sin^2\left(\frac{k_z\Delta z}{2}\right)}{(\Delta z)^2} = \frac{\sin^2\left(\frac{\omega\Delta t}{2}\right)}{(c\Delta t)^2}. \tag{18}$$

This equation is evidently different from the vacuum dispersion relation, which reads as

$$k_x^2 + k_y^2 + k_z^2 = \frac{\omega^2}{c^2}. \tag{19}$$

Comparison of the two equations shows that the dispersion characteristics are similar, if and only if $\Delta x \to 0$, $\Delta y \to 0$, $\Delta z \to 0$, and $\Delta t \to 0$. Another output of the dispersion equation is the stability condition, which is referred to as Courant-Friedrichs-Lewy (CFL) condition [26]. The spatial and temporal discretization should be related such that the term ω obtained from equation (18) has no imaginary part, i.e. $\sin^2(\omega\Delta t/2) < 1$. This implies that

$$c\Delta t < \left(\sqrt{\frac{\sin^2(\frac{k_x\Delta x}{2})}{(\Delta x)^2} + \frac{\sin^2(\frac{k_y\Delta y}{2})}{(\Delta y)^2} + \frac{\sin^2(\frac{k_z\Delta z}{2})}{(\Delta z)^2}}\right)^{-1} . \tag{20}$$

The right hand side of the above equation has its minimum when all the sinus functions are equal to one, which leads to the stability condition for the central-difference scheme:

$$\Delta t < \left(c\sqrt{\frac{1}{(\Delta x)^2} + \frac{1}{(\Delta y)^2} + \frac{1}{(\Delta z)^2}}\right)^{-1} . \tag{21}$$

As mentioned above, for the FEL simulation, it is very important to maintain the vacuum speed of light along the z direction (throughout this paper z is the electron beam and undulator direction). More accurately, if $k_x = k_y = 0$, $k_z = \omega/c$ should be the solution of the dispersion equation. However, this solution is obtained if and only if $\Delta t = \Delta z/c$, which violates the stability condition. To resolve this problem, various techniques are developed in the context of compensation of numerical dispersion. Here, we take advantage from the non-standard finite difference (NSFD) scheme to impose the speed of light propagation along z direction [35, 36].

The trick is to consider a weighted average along z for the derivatives with respect to x and y, which is formulated as follows:

$$\frac{\partial^2}{\partial x^2}\psi(x, y, z, t) \simeq \frac{\bar{\psi}^n_{i+1,j,k} - 2\bar{\psi}^n_{i,j,k} + \bar{\psi}^n_{i-1,j,k}}{(\Delta x)^2} \tag{22}$$

$$\frac{\partial^2}{\partial y^2}\psi(x, y, z, t) \simeq \frac{\bar{\psi}^n_{i,j+1,k} - 2\bar{\psi}^n_{i,j,k} + \bar{\psi}^n_{i,j-1,k}}{(\Delta y)^2}, \tag{23}$$

with

$$\bar{\psi}^n_{i,j,k} = \mathcal{A}\psi^n_{i,j,k-1} + (1 - 2\mathcal{A})\psi^n_{i,j,k} + \mathcal{A}\psi^n_{i,j,k+1}. \tag{24}$$

Such a finite difference scheme leads to the following dispersion equation:

$$\Big(1 - 4\mathcal{A}\sin^2(k_z\Delta z/2)\Big)\left(\frac{\sin^2(k_x\Delta x/2)}{(\Delta x)^2} + \frac{\sin^2(k_y\Delta y/2)}{(\Delta y)^2}\right) + \frac{\sin^2(k_z\Delta z/2)}{(\Delta z)^2} = \frac{\sin^2(\omega\Delta t/2)}{(c\Delta t)^2}. \tag{25}$$

It can be shown that if the NSFD coefficient $\mathcal{A}$ is larger than 0.25, and $\sqrt{(\Delta z/\Delta x)^2 + (\Delta z/\Delta y)^2} < 1$, a real ω satisfies the above dispersion equation for $\Delta t = \Delta z/c$. This time step additionally yields $k_z = \omega/c$, for $k_x = k_y = 0$.

The value we chose for $\mathcal{A}$ in MITHRA is obtained from

$$\mathcal{A} = 0.25\left(1 + \frac{0.02}{(\Delta z/\Delta x)^2 + (\Delta z/\Delta y)^2}\right). \tag{26}$$

The update equation can then be written as

$$\begin{aligned}\psi^{n+1}_{i,j,k} = &- \psi^{n-1}_{i,j,k} + \alpha'_1\psi^n_{i,j,k}\\ &+ \alpha'_2(\mathcal{A}\psi^n_{i+1,j,k-1} + (1-2\mathcal{A})\psi^n_{i+1,j,k} + \mathcal{A}\psi^n_{i+1,j,k+1})\\ &+ \alpha'_3(\mathcal{A}\psi^n_{i-1,j,k-1} + (1-2\mathcal{A})\psi^n_{i-1,j,k} + \mathcal{A}\psi^n_{i-1,j,k+1})\\ &+ \alpha'_4(\mathcal{A}\psi^n_{i,j+1,k-1} + (1-2\mathcal{A})\psi^n_{i,j+1,k} + \mathcal{A}\psi^n_{i,j+1,k+1})\\ &+ \alpha'_5(\mathcal{A}\psi^n_{i,j-1,k-1} + (1-2\mathcal{A})\psi^n_{i,j-1,k} + \mathcal{A}\psi^n_{i,j-1,k+1})\\ &+ \alpha'_6\psi^n_{i,j,k+1} + \alpha'_7\psi^n_{i,j,k-1} + \alpha'_8\zeta^n_{i,j,k}.\end{aligned} \tag{27}$$

where the coefficients $\alpha'_1, \ldots, \alpha'_7$ are obtained from:

$$\begin{aligned}&\alpha'_1 = 2\left[1 - (1-2\mathcal{A})\left(\left(\frac{c\Delta t}{\Delta x}\right)^2 + \left(\frac{c\Delta t}{\Delta y}\right)^2\right) - \left(\frac{c\Delta t}{\Delta z}\right)^2\right],\\ &\alpha'_2 = \alpha'_3 = \left(\frac{c\Delta t}{\Delta x}\right)^2, \qquad \alpha'_4 = \alpha'_5 = \left(\frac{c\Delta t}{\Delta y}\right)^2,\\ &\alpha'_6 = \alpha'_7 = \left(\frac{c\Delta t}{\Delta z}\right)^2 - 2\mathcal{A}\left(\left(\frac{c\Delta t}{\Delta x}\right)^2 + \left(\frac{c\Delta t}{\Delta x}\right)^2\right),\\ &\alpha'_8 = (c\Delta t)^2.\end{aligned} \tag{28}$$

To guarantee a dispersion-less propagation along z direction with the speed of light the update time step is automatically calculated from the given longitudinal discretization (Δz), according to $\Delta t = \Delta z/c$.

2.1.4. FDTD for Scalar Potential

Usually, due to high energy of particles in a FEL process, the FEL simulations neglect the space-charge effects by considering $\varphi \simeq 0$ [14]. However, this is an approximation which we try to avoid in MITHRA. To account for space-charge forces, one needs to solve the wave equation for scalar potential, i.e. (7). For this purpose, the same formulation as used for the vector potential is utilized to update the scalar potential. Nonetheless, since the position of particles are sampled at $t+\Delta t/2$ instants, the obtained value for φ^n corresponds to the scalar potential at $(n + 1/2)\Delta t$. This point should be particularly taken into consideration, when electromagnetic fields $\boldsymbol{E}$ and $\boldsymbol{B}$ are evaluated.

2.1.5. Boundary Truncation

In order to simulate the FEL problem, we consider a cube as our simulation domain. The absorbing boundary condition is also considered for updating the scalar electric potential φ at the boundaries. Therefore, we introduce the parameter ξ, which denotes either ψ or φ. The six boundaries of the cube are supposed to be at: $x = \pm l_x/2$, $y = \pm l_y/2$ and $z = \pm l_z/2$. In the following, we only present the formulation for the boundary conditions at $z = \pm l_z/2$. The process to extract the equations for the other four boundaries will be exactly similar.

First Order ABCs: The partial differential equations implying first order ABCs at $z = \pm l_z/2$ are:

$$\mp\frac{\partial^2\xi}{\partial z\partial t} - \frac{1}{c}\frac{\partial^2\xi}{\partial t^2} = 0 \tag{29}$$

Second Order ABCs: The partial differential equations implying second order ABCs at $z = \pm l_z/2$ are:

$$\mp\frac{\partial^2\xi}{\partial z\partial t} - \frac{1}{c}\frac{\partial^2\xi}{\partial t^2} - \frac{c}{2}\frac{\partial^2\xi}{\partial x^2} - \frac{c}{2}\frac{\partial^2\xi}{\partial y^2} = 0 \tag{30}$$

Particular attention should be devoted to the implementation of Mur second order absorbing boundary condition at edges and corners. Separate usage of the above equations for second order case encounters problems in the formulation. On one hand, unknown values at grid points outside the computational domain appears in the equations, and on the other a system of overdetermined equations will be obtained. The solution to this problem is to discretize all the involved boundary conditions at the center of the cubes (for corners) or squares (for edges). A simple addition of the obtained equations cancels out the values outside the computational domain and returns the desired value meeting the considered absorbing boundary condition. The first and second order Mur boundary condition gradually lose their accuracy in absorbing the incident field when large angles of incidence are involved. For this purpose, in an FEL simulation using MITHRA, boundaries need to be considered far enough from the radiating particles to decrease the effect of boundary truncation on the simulation accuracy.

2.2. *Particle In Cell (PIC)*

Particle in cell (PIC) method is the standard algorithm to solve for the bunch dynamics within an electromagnetic field distribution. The method discretizes the bunch 6D distribution function as an ensemble of macro-particles, takes the time domain data of the electric and magnetic fields, and updates the macro-particle position and momentum using a proper particle-pusher technique. We comment that the electromagnetic fields in the motion equation are the total fields in the computational domain, which in a FEL problem is equivalent to the superposition of undulator field, radiated field and the seeded field in case of a seeded FEL problem. Often considering all the individual particles involved in the problem ($\sim 10^6 - 10^9$ particles) leads to high computation costs and long simulation times. The clever solution to this problem is the macro-particle assumption, through which an ensemble of particles ($\sim 10^2 - 10^4$ particles) are treated as one single entity with charge to mass ratio equal to the particles of interest, which are here electrons. The relativistic equation of motion for electron macro-particles then reads as

$$\frac{\partial}{\partial t}(\gamma m\boldsymbol{v}) = -e(\boldsymbol{E} + \boldsymbol{v} \times \boldsymbol{B}), \qquad \text{and} \qquad \frac{\partial \boldsymbol{r}}{\partial t} = \boldsymbol{v}, \quad (31)$$

where $\boldsymbol{r}$ and $\boldsymbol{v}$ are the position and velocity vectors of the electron, e is the electron charge and m is its rest mass. γ stands for the Lortenz factor of the moving particle.

2.2.1. *Update Algorithm*

There are numerous update algorithms proposed for the time domain solution of (31), including various Runge-Kutta and finite difference algorithms. Among these methods, Boris scheme has garnered specific attention owing to its interesting peculiarity which is being simplectic. Simplectic update algorithms are update procedures which maintain the conservation of any parameter in the equation which obey a physical conservation law. Since in a FEL problem effect of the magnetic field on a particle motion plays the most important role, using a simplectic algorithm is essential to obtain reliable results. This was the main motivation to choose the Boris scheme for updating the particle motion in MITHRA.

We sample the particle position at times $m\Delta t_b$, which is represented by $\boldsymbol{r}^m$ and the particle normalized momentum at times $(m-\frac{1}{2})\Delta t_b$ which is written as $\gamma\boldsymbol{\beta}^{m-1/2}$. Then, by having $\boldsymbol{r}^m$ and $\gamma\boldsymbol{\beta}^{m-1/2}$ as the known parameters and $\boldsymbol{E}_t^m$ and $\boldsymbol{B}_t^m$ as the *total* field values imposed on the particle at instant $m\Delta t$, the values $\boldsymbol{r}^{m+1}$ and $\gamma\boldsymbol{\beta}^{m+1/2}$ are obtained as follows:

$$\begin{aligned}
\boldsymbol{t}_1 &= \gamma\boldsymbol{\beta}^{m-1/2} - \frac{e\Delta t_b \boldsymbol{E}_t^m}{2mc} \\
\boldsymbol{t}_2 &= \boldsymbol{t}_1 + \alpha\boldsymbol{t}_1 \times \boldsymbol{B}_t^m \\
\boldsymbol{t}_3 &= \boldsymbol{t}_1 + \boldsymbol{t}_2 \times \frac{2\alpha\boldsymbol{B}_t^m}{1 + \alpha^2 \boldsymbol{B}_t^m \cdot \boldsymbol{B}_t^m} \\
\gamma\boldsymbol{\beta}^{m+1/2} &= \boldsymbol{t}_3 - \frac{e\Delta t_b \boldsymbol{E}_t^m}{2mc} \\
\boldsymbol{r}^{m+1} &= \boldsymbol{r}^l + \frac{c\Delta t_b \gamma\boldsymbol{\beta}^{m+1/2}}{\sqrt{1 + \gamma\boldsymbol{\beta}^{m+1/2} \cdot \gamma\boldsymbol{\beta}^{m+1/2}}}
\end{aligned} \qquad (32)$$

with $\alpha = -e\Delta t_b/(2m\sqrt{1 + \boldsymbol{t}_1 \cdot \boldsymbol{t}_1})$. $\boldsymbol{E}_t^m = \boldsymbol{E}_{ext}^m + \boldsymbol{E}^m$ and $\boldsymbol{B}_t^m = \boldsymbol{B}_{ext}^m + \boldsymbol{B}^m$ are total fields imposed on the particle, which are equal to the superposition of the radiated field with the external fields, i.e. the undulator or the seed fields. In order to figure out the derivation of the equations (32), the reader is referred to [37, 38]. As seen from the above equations, the electric and magnetic fields at time $m\Delta t_b$ and the position $\boldsymbol{r}$ of the particle are needed to update the motion. In the next section, the equations to extract these values from the computed values of the magnetic and scalar potential are presented. Note that to achieve a certain precision level, the required time step in updating the bunch properties (Δt_b) is usually much smaller than the time step for field update (Δt). In MITHRA, there exists the possibility for setting different time steps for PIC and FDTD algorithms.

2.2.2. *Field Evaluation*

As described in section 2.1, the propagating fields in the computational domain are evaluated by solving the wave equation for the magnetic vector potential, i.e. (6). To update the particle position and momentum, one needs to obtain the field values $\boldsymbol{E}^m$ and $\boldsymbol{B}^m$ from the potentials $\boldsymbol{A}$ and φ. For this purpose, the equations (8) and (9) need to be discretized in a consistent manner to provide the accelerating field with lowest amount of dispersion and instability error. First, the values of magnetic and scalar potentials at $t+\Delta t/2$ are used to evaluate the electromagnetic fields at the cell vertices. Subsequently, the field values are interpolated to the particle location for updating the equation of motion. An important consideration at this stage is compatible interpolation of fields from the cell vertices with the interpolations used for current and charge densities. Similar interpolation algorithms should be followed to cancel the effect of self-forces on particle motion.

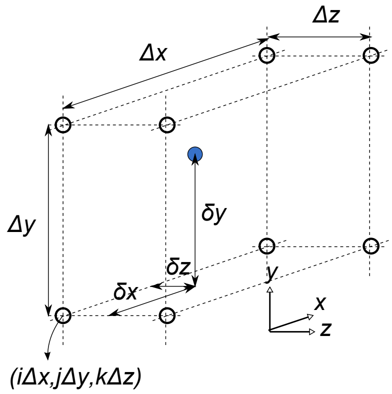

Figure 1: Schematic illustration of the parameters used to locate a particle within the computational domain.

Using the equation (8), the magnetic field $\boldsymbol{B}^n_{i,j,k}$ at cell vertex (i, j, k) is calculated as follows:

$$B_{x_{i,j,k}}^{n} = \frac{1}{2}\left(\frac{A_{z_{i,j+1,k}}^{n} - A_{z_{i,j-1,k}}^{n}}{2\Delta y} - \frac{A_{y_{i,j,k+1}}^{n} - A_{y_{i,j,k-1}}^{n}}{2\Delta z} + \frac{A_{z_{i,j+1,k}}^{n+1} - A_{z_{i,j-1,k}}^{n+1}}{2\Delta y} - \frac{A_{y_{i,j,k+1}}^{n+1} - A_{y_{i,j,k-1}}^{n+1}}{2\Delta z}\right), \tag{33}$$

$$B_{y_{i,j,k}}^{n} = \frac{1}{2}\left(\frac{A_{x_{i,j,k+1}}^{n} - A_{x_{i,j,k-1}}^{n}}{2\Delta z} - \frac{A_{z_{i+1,j,k}}^{n} - A_{z_{i-1,j,k}}^{n}}{2\Delta x} + \frac{A_{x_{i,j,k+1}}^{n+1} - A_{x_{i,j,k-1}}^{n+1}}{2\Delta z} - \frac{A_{z_{i+1,j,k}}^{n+1} - A_{z_{i-1,j,k}}^{n+1}}{2\Delta x}\right), \tag{34}$$

$$B_{z_{i,j,k}}^{n} = \frac{1}{2}\left(\frac{A_{y_{i+1,j,k}}^{n} - A_{y_{i-1,j,k}}^{n}}{2\Delta x} - \frac{A_{x_{i,j+1,k}}^{n} - A_{x_{i,j-1,k}}^{n}}{2\Delta y} + \frac{A_{y_{i+1,j,k}}^{n+1} - A_{x_{i-1,j,k}}^{n+1}}{2\Delta x} - \frac{A_{x_{i,j+1,k}}^{n+1} - A_{x_{i,j-1,k}}^{n+1}}{2\Delta y}\right). \tag{35}$$

Similarly, equation (9) is employed to evaluate the electric field at the cell vertices. The electric field $\boldsymbol{E}^n_{i,j,k}$ is obtained from the following equations:

$$E_{x_{i,j,k}}^{n} = \left(-\frac{A_{x_{i,j,k}}^{n+1} - A_{x_{i,j,k}}^{n}}{\Delta t} - \frac{\varphi^n_{i+1,j,k} - \varphi^n_{i-1,j,k}}{2\Delta x}\right), \tag{36}$$

$$E_{y_{i,j,k}}^{n} = \left(-\frac{A_{y_{i,j,k}}^{n+1} - A_{y_{i,j,k}}^{n}}{\Delta t} - \frac{\varphi^n_{i,j+1,k} - \varphi^n_{i,j-1,k}}{2\Delta y}\right), \tag{37}$$

$$E_{z_{i,j,k}}^{n} = \left(-\frac{A_{z_{i,j,k}}^{n+1} - A_{z_{i,j,k}}^{n}}{\Delta t} - \frac{\varphi^n_{i,j,k+1} - \varphi^n_{i,j,k-1}}{2\Delta z}\right). \tag{38}$$

Suppose that a particle resides at the cell ijk with the grid point indices shown in Fig. 1. As illustrated in Fig.1, the distance to the corner $(i\Delta x, j\Delta y, k\Delta z)$ is assumed to be $(\delta x, \delta y, \delta z)$. We use a linear interpolation of the fields from the vertices to the particle position to calculate the imposed field. If ς denotes for a component of the electric or magnetic field, i.e. $\varsigma \in \{E_x, E_y, E_z, B_x, B_y, B_z\}$, one can write

$$\varsigma^p = \sum_{I,J,K}\left(\frac{1}{2} + (-1)^I\left|\frac{1}{2} - \frac{\delta x}{\Delta x}\right|\right)\left(\frac{1}{2} + (-1)^J\left|\frac{1}{2} - \frac{\delta y}{\Delta y}\right|\right)\left(\frac{1}{2} + (-1)^K\left|\frac{1}{2} - \frac{\delta z}{\Delta z}\right|\right)\varsigma_{i+I,j+J,k+K}, \tag{39}$$

where I, J, and K are equal to either 0 or 1, producing the eight indices corresponding to the eight corners of the mesh cell.

2.2.3. *Current Deposition*

Once the position and momentum of all the particles over the time interval Δt is known, one needs to couple the pertinent currents into the wave equation (6). As described before, this coupling over time is implemented through the equation (16). The remaining question is how to evaluate the related currents on the grid points, i.e. the method for performing an spatial interpolation. To maintain consistency, we should use a similar interpolation scheme as used for the field evaluation. This assumption leads to the following equation for spatial interpolation.

$$\rho^p{}_{i+I,j+J,k+K} = \rho\left(\frac{1}{2} + (-1)^I\left|\frac{1}{2} - \frac{\delta x}{\Delta x}\right|\right)\left(\frac{1}{2} + (-1)^J\left|\frac{1}{2} - \frac{\delta y}{\Delta y}\right|\right)\left(\frac{1}{2} + (-1)^K\left|\frac{1}{2} - \frac{\delta z}{\Delta z}\right|\right) \tag{40}$$

where ρ is the charge density attributed to each macroparticle, namely $q/(\Delta x \Delta y \Delta z)$. $\rho^p{}_{i,j,k}$ is the charge density at the grid point (i, j, k) due to the moving particle p in the computational mesh cell (Fig. 1a). I, J, and K are equal to either 0 or 1, which produce the eight indices corresponding to the eight corners of the mesh cell. The total charge density $\rho_{i,j,k}$ will be a superposition of all the charge densities due to the moving particles of the bunch. We have removed the superscripts corresponding to the time instant, to avoid the confusion due to different time marching steps Δt and Δt_b. The above interpolation is carried out at each update step of the field values. One can consider the above interpolation equations as a rooftop charge distribution centered at the particle position and expanding in the regions $(-\Delta x < x < \Delta x, -\Delta y < y < \Delta y, -\Delta z < z < \Delta z)$.

Eventually, equation (16) is used to calculate the corresponding current densities.

The combination of equation (16) and (40) should maintain the charge conservation law (equation (10)) in a discretized space. For this purpose, the projection from position vectors $\boldsymbol{r}$ to the Cartesian components in (16) should be done using the so-called ZigZag scheme proposed in [34]. According to this scheme when a particle moves from the point (x_1, y_1, z_1) to (x_2, y_2, z_2), the motion is divided into two separate movements, namely (i) from (x_1, y_1, z_1) to (x_r, y_r, z_r), and (ii) from (x_r, y_r, z_r) to (x_2, y_2, z_2). The coordinates of the relay point (x_r, y_r, z_r) are obtained from the following equation:

$$\begin{aligned} x_r &= \min\Big[\, \min(i_1\Delta x, i_2\Delta x) + \Delta x, \\ &\qquad \max\Big(\max(i_1\Delta x, i_2\Delta x), \frac{x_1 + x_2}{2}\Big)\Big] \\ y_r &= \min\Big[\, \min(j_1\Delta y, j_2\Delta y) + \Delta y, \\ &\qquad \max\Big(\max(j_1\Delta y, j_2\Delta y), \frac{y_1 + y_2}{2}\Big)\Big] \qquad (41) \\ z_r &= \min\Big[\, \min(k_1\Delta z, k_2\Delta z) + \Delta z, \\ &\qquad \max\Big(\max(k_1\Delta z, k_2\Delta z), \frac{z_1 + z_2}{2}\Big)\Big] \end{aligned}$$

where (i, j, k) with indices 1 and 2 represent the cell numbers containing the initial and final points, respectively. Since potential $\boldsymbol{A}$ and φ are obtained from current and charge in exactly similar ways (update equations), if charge and current obey the charge conservation, the gauge condition will be automatically satisfied. In other words, if the initial potentials satisfy the gauge condition, solving equations (6), (7), and (10) results in potential distributions at time t which also satisfy the gauge condition. The only requirement is that both potentials are discretized and updated in the same way.

2.3. *Quantity Initialization*

The previous two sections on FDTD and PIC algorithms present a suitable and efficient framework for the computation of interaction between charged particles and propagating waves. However, the initial conditions are always required for a complete determination of the problem of interest. For a FEL simulation, the initial conditions corresponding to the FEL input are given to the FDTD/PIC solver. For example, in case of a SASE (Self Amplified Spontaneous Emission) FEL, the initial fields are zero and there is no excitation entering the computational domain, whereas for a seeded FEL, an outside excitation should be considered entering the computational domain. The explanation of how such initializations are implemented in MITHRA is the goal in this section.

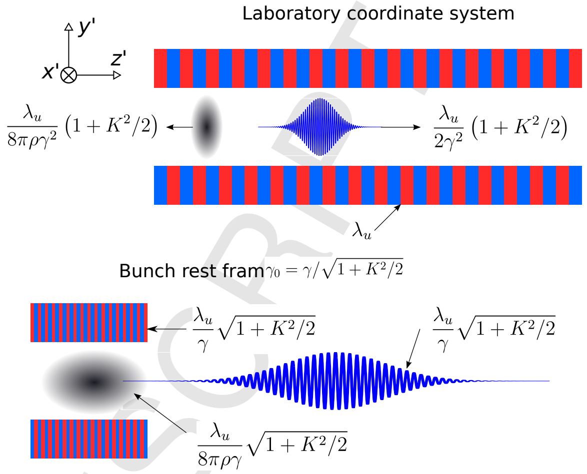

Figure 2: Schematic illustration of the Lorentz boosting to transform the problem from the laboratory frame to the bunch rest frame.

One novel feature of the method, followed here, is the solution of Maxwell's equations in the bunch rest frame. It can be shown that a proper coordinate transformation yields the matching of all the major parameters in a FEL simulation, namely bunch length, undulator period, undulator length, and radiation wavelength. Fig. 2 schematically describes the advantage of moving into the bunch rest frame. In a typical FEL problem, the FEL parameter ρ_{FEL} is about 10^{-3}. Therefore, simulation of FEL interaction with a bunch equal to the cooperation length of the FEL ($L_c = \lambda_l/(4\pi\rho_{FEL})$, with λ_l being the radiation wavelength) requires a simulation domain only 100 times larger than the wavelength. This becomes completely possible with the today computer technology and constitutes the main goal of MITHRA. In this section, the main basis for Lorentz boosting the simulation coordinate is described first. Afterwards, the relations for evaluating the undulator fields in the Lorentz boosted framework are presented. Finally, the electron bunch initialization in the Lorentz-boosted framework is discussed.

2.3.1. *Lorentz Transformation*

It is known from the FEL thoery that a bunch with central Lorentz factor equal to γ moves in an undulator with an average Lorentz factor equal to $\gamma_0 = \gamma/\sqrt{(1 + K^2/2)}$, where $K = eB\lambda_u/(2\pi mc)$ is the undulator parameter determining the amplitude of the wiggling motion. Consequently, a frame moving with normalized velocity $\beta_0 = \sqrt{1 - 1/\gamma_0^2}$ is indeed the bunch rest frame, where the volume of the computational domain stays minimal. Transforming into this coordinate system necessitates tailoring the bunch and undulator properties. For this purpose, the Lorentz length contraction, time dilation and relativistic velocity addition need to be employed.

In MITHRA, the input parameters are all taken in the laboratory frame and the required Lorentz transformations are carried out based on the bunch energy. The required transformations for the computational mesh are as the following:

$$\Delta z = \Delta z' \gamma_0, \tag{42}$$

$$\Delta t = \Delta t' / \gamma_0, \tag{43}$$

$$\Delta t_b = \Delta t'_b / \gamma_0, \tag{44}$$

where the prime sign stands for the quantities in the laboratory frame. The quantities without prime are values in the bunch rest frame, which are used in the FDTD/PIC simulation. With the consideration of the above transformations, the length of the total computational domain along the undulator period and the total simulation time is also transformed similarly.

In addition to the data for the computational mesh, the properties of the electron bunch also changes after the Lorentz boosting. This certainly affects the bunch initialization process which is thoroughly explained in the next section. An electron bunch in MITHRA is initialized and characterized by the following parameters:

(i) Mean electron position: $(\bar{x}_b, \bar{y}_b, \bar{z}_b)$,

(ii) Mean electron normalized momentum: $(\overline{\gamma\beta}_x, \overline{\gamma\beta}_y, \overline{\gamma\beta}_z)$,

(iii) RMS value of the electron position distribution: $(\sigma_x, \sigma_y, \sigma_z)$,

(iv) RMS value of the electron normalized momentum distribution: $(\sigma_{\gamma\beta_x}, \sigma_{\gamma\beta_y}, \sigma_{\gamma\beta_z})$.

As mentioned previously, the above parameters are entered by the user in the laboratory frame. To transform the given values to the bunch rest frame the position related parameters are changed as

$$\begin{aligned} \bar{x}_b &= \bar{x}'_b, \quad \bar{y}_b = \bar{y}'_b, \quad \bar{z}_b = \frac{\bar{z}'_b}{\gamma_0(1-\bar{\beta}'_z\beta_0)}, \\ \sigma_x &= \sigma'_x, \quad \sigma_y = \sigma'_y, \quad \sigma_z = \frac{\sigma'_z}{\gamma_0(1-\bar{\beta}'_z\beta_0)}. \end{aligned} \tag{45}$$

To transfer the momentum related quantities, we assume that the main contribution to the Lorentz factor is the momentum along z direction or the undulator period. In other words, $(\overline{\gamma\beta}_x, \overline{\gamma\beta}_y, \overline{\gamma\beta}_z) = \gamma(\bar{\beta}_x, \bar{\beta}_y, \bar{\beta}_z)$, with $\gamma = 1/\sqrt{1-\bar{\beta}_z^2}$. Similarly, the RMS values can also be written as $(\sigma_{\gamma\beta_x}, \sigma_{\gamma\beta_y}, \sigma_{\gamma\beta_z}) = \gamma(\sigma_{\beta_x}, \sigma_{\beta_y}, \sigma_{\beta_z})$. Using the relativistic velocity transformation [39], the transformation equations for the above values are found as follows:

$$\gamma = \gamma'\gamma_0(1-\bar{\beta}'_z\beta_0), \tag{46}$$

$$(\bar{\beta}_x, \bar{\beta}_y, \bar{\beta}_z) = (\bar{\beta}'_x, \bar{\beta}'_y, \sqrt{1-1/\gamma^2}), \tag{47}$$

$$(\sigma_{\gamma\beta_x}, \sigma_{\gamma\beta_y}, \sigma_{\gamma\beta_z}) = (\sigma'_{\gamma\beta_x}, \sigma'_{\gamma\beta_y}, \sigma'_{\gamma\beta_z})\gamma_0(1-\bar{\beta}'_z\beta_0). \tag{48}$$

Equations (42)-(48) provide a sufficient set of equations to perform the Lorentz boost to the bunch rest frame.

2.3.2. Field Initialization

The utilized FDTD/PIC algorithm solves the Maxwell's equation coupled with the motion equation of an ensemble of particles. Therefore, in addition to the field values, particle initial conditions should also be initialized. For a SASE FEL problem, the initial field profile is zero everywhere, whereas for a seeded FEL the initial seed should enter the computational domain through the boundaries. In both cases, the external field which is the undulator field should separately be initialized.

Undulator Field: By solving the Laplace equation for the magnetic field, the undulator field in the laboratory frame is found to be as the following (Fig. 2) [1]:

$$\begin{aligned} B'_x &= 0, \\ B'_y &= B_0 \cosh(k_u y') \sin(k_u z'), \\ B'_z &= B_0 \sinh(k_u y') \cos(k_u z'), \end{aligned} \tag{49}$$

where B_0 is the maximum transverse field of the undulator. To calculate the undulator field in the bunch rest frame, first the position is transformed to laboratory frame (x', y', z') through the Lorentz boost equations. Afterwards, the field is evaluated using the equation (49). Eventually, these fields are transformed back into the bunch rest frame. The above approach, although adds few mathematical operations for the calculation of undulator fields, it enables straightforward implementation of various realistic effects, like fringing fields of the entrance section and non-gaussian field profiles.

An important consideration in the initialization of undulator field is the entrance region of the undulator. A direct usage of the equation (49) with zero field for $z' < 0$ causes an abrupt variation in the particles motion, which results in a spurious coherent radiation. In fact, in a real undulator, there exists fringing fields at the undulator entrance, which remove any abrupt transition in the undulator field and consequently the particle radiations [40]. To the best of our knowledge, the fringing fields are always modeled numerically and there exists no analytical solution for the problem. Here, we approximate the fringing fields by a gradually decreasing magnetic field in form of a Neumann function. The coefficients in the function are set such that the particles do not gain any net transverse momentum and stay in the computational domain as presumed. The undulator field for $z' < 0$ in the laboratory frame is obtained as the following:

$$\begin{aligned} B'_x &= 0, \\ B'_y &= B_0 \cosh(k_u y') k_u z' e^{-(k_u z')^2/2}, \\ B'_z &= B_0 \sinh(k_u y') e^{-(k_u z')^2/2}, \end{aligned} \tag{50}$$

The same transformations as in (49) can be used to approximate the fringing field values in the bunch rest frame.

Seed Field: External excitation of free electron laser process using a seed mechanism has proved to be advantageous in terms of output spectrum, photon flux and the required undulator length [41, 1]. Such benefits has propelled the proposal of seeded FEL schemes. To simulate such a mechanism, MITHRA uses the TF/SF (total-field/scattered-field) technique to introduce an external excitation into the computational domain. When seeding is enabled by having a non-zero seed amplitude, the second and third points (after the boundary points) constitute the scattered and total field boundaries, respectively. Therefore, during the time marching process, after each update according to equation (27) the excitation terms are added to the fields at TF/SF boundaries. For example for the TF/SF boundaries close to $z = z_{min}$ plane, the field values to be used in the next time steps are obtained as the following:

SF boundary:

$$\begin{aligned} \psi'^{n+1}_{i,j,k} &= \psi^{n+1}_{i,j,k} + \mathcal{A}(\alpha'_2 f^n_{i+1,j,k+1} + \alpha'_3 f^n_{i-1,j,k+1} + \alpha'_4 f^n_{i,j+1,k+1} \\ &+ \alpha'_5 f^n_{i,j-1,k+1}) + \alpha'_6 f^n_{i,j,k+1}, \end{aligned}$$

TF boundary:

$$\begin{aligned} \psi'^{n+1}_{i,j,k} &= \psi^{n+1}_{i,j,k} - \mathcal{A}(\alpha'_2 f^n_{i+1,j,k-1} + \alpha'_3 f^n_{i-1,j,k-1} + \alpha'_4 f^n_{i,j+1,k-1} \\ &+ \alpha'_5 f^n_{i,j-1,k-1}) - \alpha'_7 f^n_{i,j,k-1}, \end{aligned} \tag{51}$$

where $f^n_{i,j,k}$ is the excitation value at time $n\Delta t$ and position $(i\Delta x, j\Delta y, k\Delta z)$. The excitation value is calculated based on the imposed seed fields, which are usually either a plane wave or a Gaussian beam radiation.

2.3.3. Electron Bunch Generation

Position and momentum initialization: As described previously, the evolution of the electron bunch is always simulated by following the macro-particle approach, where an ensemble of particles are represented by one sample particle. This typically reduces the amount of computation cost for updating the bunch properties by three or four orders of magnitude. Due to the high sensitivity of a FEL problem to the initial conditions, correct and proper initialization of these macro-particles play a critical role in obtaining reliable results. In computational accelerator physics, different approaches are introduced and developed for bunch generation. Some examples are random generation of particles, mirroring macro-particles at different phases to prevent initial average bunching factors, and independent random filling of different coordinates to prevent unrealistic correlations [42]. Among all the different methods, using the sophisticated methods to load the bunch in a ”quasi-random” manner seem to be the most appropriate solutions. The Halton or Hammersley sequences, as generalizations of the bit-reverse techniques, are implemented in MITHRA for particle generation. These sequences compared to random based filling of the phase space avoid the appearance of local clusters in the bunch distribution. In addition, the uniform filling of the phase space prevents initial bunching factor of the generated electron bunch, making it well-suited for FEL simulations.

For details on the nature of Halton sequences, the reader is referred to the specialized documents. By having the above uniform distributions, the 6D phase space of the initial bunch can be filled according to the desired bunch properties.

In MITHRA, different schemes for the user is implemented to generate the initial electron bunch. The main requirements for initializing the bunches is to generate 1D and 2D set of numbers with either uniform or Gaussian distributions. Suppose x_1 and x_2 are two uncorrelated number sequences produced by the Halton algorithm. A 1D uniform distribution y_1 with average y_{m1} and total width y_{s1} is found by the following transformation:

$$y_1 = y_{s1}(x_1 - \frac{1}{2}) + y_{m1}. \tag{52}$$

Such a distribution is used when a bunch with uniform current profile (z distribution of particles) is to be initialized. On the other hand, a 1D Gaussian distribution is needed when radiation of a bunch with Gaussian current profile is modelled. To generate bunches with Gaussian distribution, we employ Box-muller’s theory to extract a sequence of numbers with Gaussian distribution from two uncorrelated uniform distributions. Based on this theory, a 1D Gaussian distribution y_2 with average y_{m2} and deviation width y_{s2} is found by the following transformation:

$$y_2 = y_{s2}\sqrt{-2\ln x_1}\cos(2\pi x_2) + y_{m2}. \tag{53}$$

Similar to the undulator fields, an abrupt variation in the bunch profile results in an unrealistic coherent scattering emission (CSE), which happens if the uniform bunch distribution is directly initialized from equation (52). CSE is avoided by imposing smooth variations in the particle distribution. For this purpose, a small Gaussian bunch with the same density as the real bunch and a width equal to an undulator wavelength is produced. The lower half of the bunch (particles with smaller z) is transferred to the tail and the other half is placed at the head of the uniform bunch. Hence, a uniform current profile with smooth variations at its head and tail is created.

The transverse coordinates of the bunches are initialized using 2D distributions. In MITHRA, a 2D Gaussian distribution is assumed for transverse coordinates. To generate such a distribution, two independent sets of numbers x_1 and x_2 are generated based on Halton sequence. The desired 2D Gaussian distribution with average position (y_{m3}, y_{m4}) and total deviation (y_{s3}, y_{s4}) is produced as the following:

$$\begin{aligned} y_3 &= y_{s3}\sqrt{-2\ln x_1}\cos(2\pi x_2) + y_{m3}, \\ y_4 &= y_{s4}\sqrt{-2\ln x_1}\sin(2\pi x_2) + y_{m4}. \end{aligned} \tag{54}$$

Such algorithms are similarly used to generate the distribution in particle momenta. The only difference is that for initializing a distribution in momentum merely Gaussian profiles are considered in transverse and longitudinal coordinates.

Bunching factor: Free electron laser radiation should start from a nonzero initial radiation. This radiation can be in form of an initial seed field, initial modulation in the bunch, or the radiation from bunch shot noise. In the current version of MITHRA, we have implemented the first two types. The implementation of shot noise is postponed to the next versions of the software. The implementation of seeding through an external excitation using TF/SF boundaries was described in 2.3.2. Here, we explain how an initial bunching factor, $< e^{jk_u z} >$, is introduced to the electron bunch profile.

For this purpose, we follow the procedure proposed in [43] and [42]. A small variation δz is applied to a particle distribution, which is generated using the above formulations. δz for each particle is obtained from

$$\delta z = \xi\gamma_0 k_u b_f \sin(2\xi\gamma_0 k_u z), \tag{55}$$

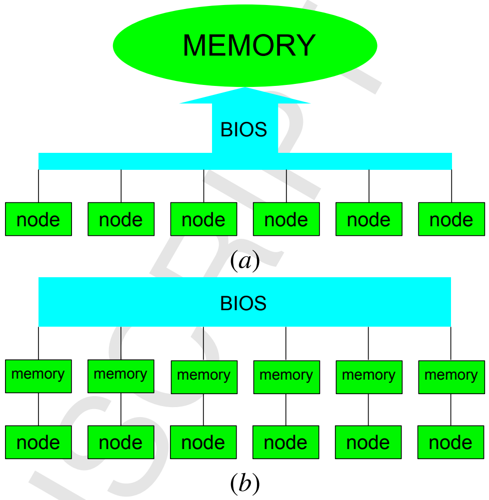

Figure 3: Schematic illustration of the (a) shared and (b) distributed memory parallelization schemes.

where b_f is the given bunching factor of the distribution, and $\xi = 1 + \bar{\beta}_z/\beta_0$ accounts for the change in the bunch longitudinal velocity after entering the undulator. The introduced variation to the bunch coordinates, i.e. $z \to z + \delta z$, yields a bunch with all the given particle and momentum distributions and the desired bunching factor, b_f.

2.4. Parallelization

The large and demanding computation cost needed for the simulation of the FEL process even in the Lorentz boosted coordinate frame necessitates solving the problem on multiple processors to achieve reasonable computation times. Therefore, efficient parallelization techniques should be implemented in the FDTD/PIC algorithm to develop an efficient software. Traditionally, there are two widely used techniques to run a computation in parallel on several processors: (1) *shared* memory, and (2) *distributed* memory parallelization. In the shared memory parallelization or the so-called multi-threading technique, several processors run a code using the variables saved in one shared memory (Fig. 3a). This technique is very suitable for PIC algorithms because it avoids the additional costs of communicating the particle position and momenta between the processors. On the other hand, distributed memory technique distributes the involved variables among several processors, solves the problem in each processor independently and communicates the required variables whenever they are called (Fig. 3b). The distributed memory technique is very suitable for FDTD algorithm due to the ease of problem decomposition beyond vari-

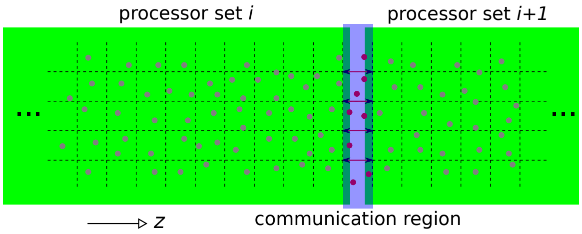

Figure 4: Schematic illustration of the domain decomposition used for distributed memory parallelization in MITHRA

ous machines. The advantage is fast reading and writing of the data and the possibility to share the computational load between different machines.

Choosing a suitable parallelization scheme for the hybrid FDTD/PIC algorithm depends on both problem size and machine implementations. Therefore, both techniques are implemented in the software and finding an efficient distribution of the computational task among the available processors is offered to the user. More accurately, the user has the possibility to determine how many processors are threaded (shared memory) and how far the multi-threaded algorithm is parallelized among separate processors. The multi-threading parallelization in MITHRA is implemented using OpenMP package. The implementation simply requires distributing the loops among different threads along with certain considerations to avoid race conditions. The total computational domain is then decomposed to several separate regions, each of them solved by one set of multi-threaded processors. These sets of processors communicate the required variables based on the technique visualized in Fig. 4.

To parallelize the computation among N sets of multi-threaded processors, the whole computational domain is divided into N domains along z (undulator period) axis. In each time update of the field, the field values at the boundaries of each domain are communicated with the corresponding processor set. To parallelize the PIC solver, we define a communication domain which as shown in Fig. 4, is the region between the boundaries of each processor. After each update of the particles position, it is checked if the particle has entered a communication domain. In case of residing in the communication region, the master processor, which is the processor containing the particle in the previous time step, communicates the new coordinates to the slave processor, which is the processor sharing the communication region with the master one. Through this simple algorithm, both parallelization schemes function simultaneously to achieve the fastest computation feasible and compatible with an available computing machine.

3. Results

The goal in this section is more accurate evaluation of the pros and cons of the developed FDTD/PIC algorithm through the presented examples. For example, the computation time, numerical stability and numerical convergence and more importantly the reliability of the results are studied based on some standard examples.

3.1. Example 1: Infrared FEL

3.1.1. Problem Definition

Table 2: Parameters of the Infrared FEL configuration considered as the first example.

FEL parameter	Value
Current profile	Uniform
Bunch size	$(260\times260\times100)\,\mu$m
Bunch charge	29.5 pC
Bunch energy	51.4 MeV
Bunch current	88.5 A
Longitudinal momentum spread	0.01%
Normalized emittance	0.0
Undulator period	3.0 cm
Magnetic field	0.5 T
Undulator parameter	1.4
Undulator length	5 m
Radiation wavelength	$3\,\mu$ m
Electron density	$2.72\times10^{13}\,1/\text{cm}^3$
Gain length (1D)	22.4 cm
FEL parameter	0.006
Cooperation length	$39.7\,\mu$m
Initial bunching factor	0.01

As the first example, we consider an infrared FEL with the parameters tabulated in table 3.1.1, which is inspired by the numerical analysis presented in [7]. The bunch distribution is assumed to be uniform in order to compare the results with one-dimensional FEL theory. For the same purpose, the transverse energy spread is considered to be zero and a minimal longitudinal energy spread is assumed.

In the mesh definition, the transverse size of the computational domain is considered almost 10 times larger than the bunch transverse size. In the contrary, the longitudinal size of the mesh is only three times larger than the bunch length. This needs to be considered due to the failure of absorbing boundary conditions for the oblique incidence of the field. Furthermore, the bunch and undulator both have tapering sections (eq. (51)) to avoid abrupt transitions producing coherent scattering emission (CSE).

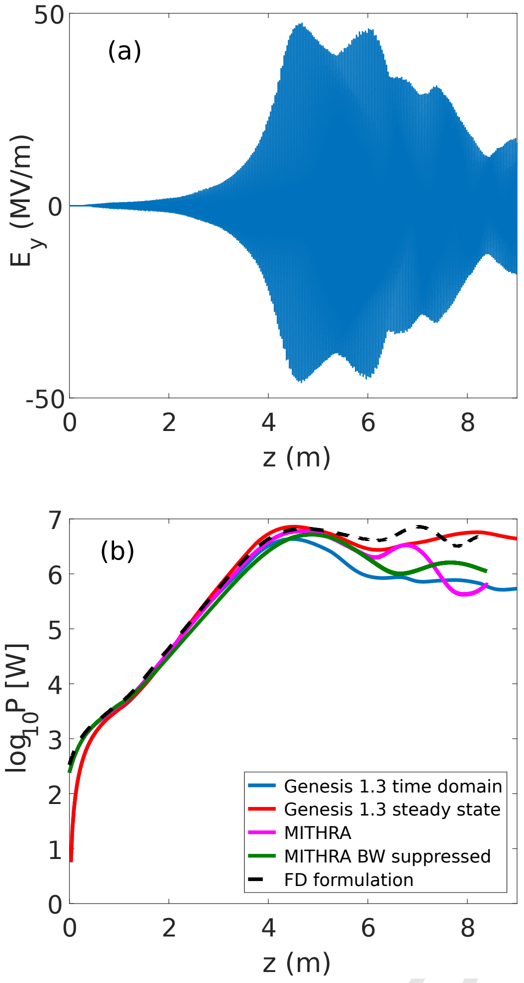

Figure 5: (a) The transverse field E_y at 110 μm distance from the bunch center and (b) the total radiated power calculated at 110 μm distance from the bunch center in terms of the traveled undulator length.

3.1.2. Simulation Results

In the beginning, we neglect the space-charge effect only to achieve a good assessment of MITHRA simulation results. The investigation of space-charge effect will be performed in the second step. Fig. 5a shows the transverse electric field sampled at 110 μm in front of the bunch center. The logarithmic plot of the radiated power for different propagation lengths (z) is also depicted in Fig. 5b. We comment that the full-wave analysis offered by MITHRA obtains the total radiated field as a superposition of forward, backward and near-field radiation components. In an FEL simulation, one is often interested in the forward radiation component, which can only be extracted at a distance in front of the radiation source, namely the electron bunch. This is the main reason for illustrating the radiated power and field at 110 μm in front of the bunch center.

According to the 1D FEL theory the gain length of the considered SASE FEL configuration is $L_G = 22.4$ cm. The gain length calculated from the slope of the power curve is $L_G = 22$ cm. There exists also a good agreement in the computed saturation power. The beam energy according to the data in table 3.1.1 is 1.52 mJ which for the bunch length of 100 μm corresponds to $P_{beam} = 4.55$ GW beam power. The estimated saturation power according to the 1D theory is equal to $P_{sat} = \rho P_{beam} = 2.7$ GW. The saturation power computed by MITHRA is 2.6 GW.

We have also performed a comparison study between the obtained results from MITHRA and the code Genesis 1.3, which is presented in Fig. 5b. As observed, both codes produce similar results in the initial state and the gain regime. Nonetheless, there exists a considerable discrepancy between the calculated radiated power in the saturation regime. The illustrated results in Fig. 5b show that the steady state and time domain analyses using Genesis do not produce similar results. This shows that the bunch is not long enough to justify the steady state approximation, and dictates a time domain analysis for accurate simulation. However, the results obtained by MITHRA at saturation do not match with the Genesis results even in the time domain.

The origin of such a discrepancy is described as follows: As explained in section 1, Genesis 1.3 and all the existing softwares for FEL simulation neglect the backward radiation of the electrons. Such an approximation is motivated by the inherent interest in forward radiation in the FEL process. However, the backward radiation although is seldom used due to its long wavelength, it influences the motion of electrons, the charge distribution and in turn the FEL output. The influence of low-frequency backward radiation on the performance of free electron lasers has been already studied in a 1D regime [44]. The effect becomes stronger in the saturation regime, when the electrons are microbunched and the FEL forward radiation is a strong function of the particles distribution. To demonstrate this effect, we changed the parallelization algorithm of the field-solver so that the propagated fields are only coupled along the FEL propagation direction. This trick suppresses the propagation of backward radiation. The results of such an analysis is also shown in Fig. 5b, which shows a relatively better agreement with time domain simulation results returned by Genesis 1.3. The still existing discrepancy is attributed to the different formulations of FDTD and TDA algorithms as well as the introduced tapers in bunch current and undulator fields.

There exists a discrepancy between MITHRA and Genesis 1.3 results at the beginning of the undulator. The reason for this discrepancy in the initial radiation is that MITHRA initializes the bunch outside the undulator. After passing through the fringing fields of the undulator, CSE happens which causes MITHRA to show the beginning of radiation from a value different from zero, whereas in Genesis 1.3 and in many of the typical FEL codes radiation starts from zero. We preferred such an operation basis in MITHRA to consider for the CSE effect in real FEL simulations. Furthermore, in Fig. 5b, we compare the results obtained using the NSFD implemented in MITHRA and standard FD scheme. As observed, formulation based on FD predicts higher radiation power compared to NSFD. This effect happens due to the smaller phase velocity of light when wave propagation follows dispersion equation (18). The result is slower phase slippage of electron bunch over the radiation and consequently later saturation of the radiation.

As a 3D electromagnetic simulation, it is always beneficial to investigate the electromagnetic field profile in the computational domain. Using the field visualization capability in MITHRA, snapshots of the field profile at different instants and from various view points are provided. In Fig. 6, snapshots of the radiated field profile at different time instants are illustrated. The emergence of lasing radiation at the end of the undulator motion is clearly observed in the field profile. We believe that the transverse modulations observed in the field profile at the end of FEL interaction are due to the transverse discretization of the spatial domain.

Furthermore, snapshots of the bunch profile are also presented beside the field profile. The main FEL principle which is the lasing due to micro-bunching of the electron bunch is observed from the field and bunch profiles. The first two snapshots evidence a considerable change in the bunch length, which occurs due to the entrance in the undulator. The bunch outside of the undulator with Lorentz factor γ travels faster than the bunch inside the undulator with Lorentz factor $\gamma/\sqrt{1+K^2/2}$. Therefore, after the entrance to the undulator the bunch length becomes shorter. This effect may not be easily observed in real laboratory frame, but is significant in electron rest frame. In addition, it is observed that some of the macro-particles escape the bunch after propagation throughout the undulator. In addition, it is observed that some of the macro-particles escape the bunch after propagation throughout the undulator. This effect is observed after space-charge effects are included in the simulation, which introduces intense transverse forces, particularly in the regions where bunch distribution is dense due to micro-bunching effect.

3.1.3. Convergence Analysis

The convergence rate of the results is one important characteristic used to assess a numerical algorithm. In our FEL analysis, there are several parameters introduced by the numerical method which may affect the final result. These parameters include (1) number of macro-particles (n), (2) time step for updating equation of motion (Δt_b), (3) longitudinal mesh size (l_z), (4) transverse mesh size ($l_x = l_y$), (5) longitudinal discretization (Δz) and (6) transverse discretization ($\Delta x = \Delta y$). Studying the convergence of the results is crucial to acquire an estimate for the uncertainty in the reported values. Here, this task is accomplished by sweeping over the above parameters and plotting the error function defined as the following:

$$\text{error} = \frac{\int_{z_i}^{z_f} |P(z) - P_0(z)| \mathrm{d}z}{\int_{z_i}^{z_f} P_0(z) \mathrm{d}z}, \tag{56}$$

where z_i and z_f are the beginning and end of the undulator, respectively and P_0 is the reference simulation result which is chosen as the results with the highest resolution.

In Fig. 7 the convergence study is shown for the aforementioned parameters. Generally, accuracy of less than 3% is achieved by using the initially suggested values.

3.1.4. Space-charge effect

A promising benefit offered by MITHRA is the assessment of various approximations used in the previously developed FEL codes. As an example, the algorithm used in the TDA method to evaluate the space-charge effect can be examined and verified using this code. The TDA method implemented in Genesis 1.3 software considers a periodic variation of space-charge force throughout the electron bunch [45, 42]. This assumption is implicitly made when electric potential equation is solved in a discrete Fourier space over one slice. The truncation of this Fourier series is equivalent to the periodic repetition of the simulation domain. However, a simple investigation of bunch profiles shown in Fig. 6c shows that a periodic assumption for the electron distribution may be a crude approximation. In addition, this assumption is favored by the FEL gain process and potentially decreases any detrimental influence of the space-charge fields on the FEL radiation. On the other hand, the algorithm in TDA method considers longitudinal space-charge forces and neglects transverse forces, which is merely valid in high energy electron

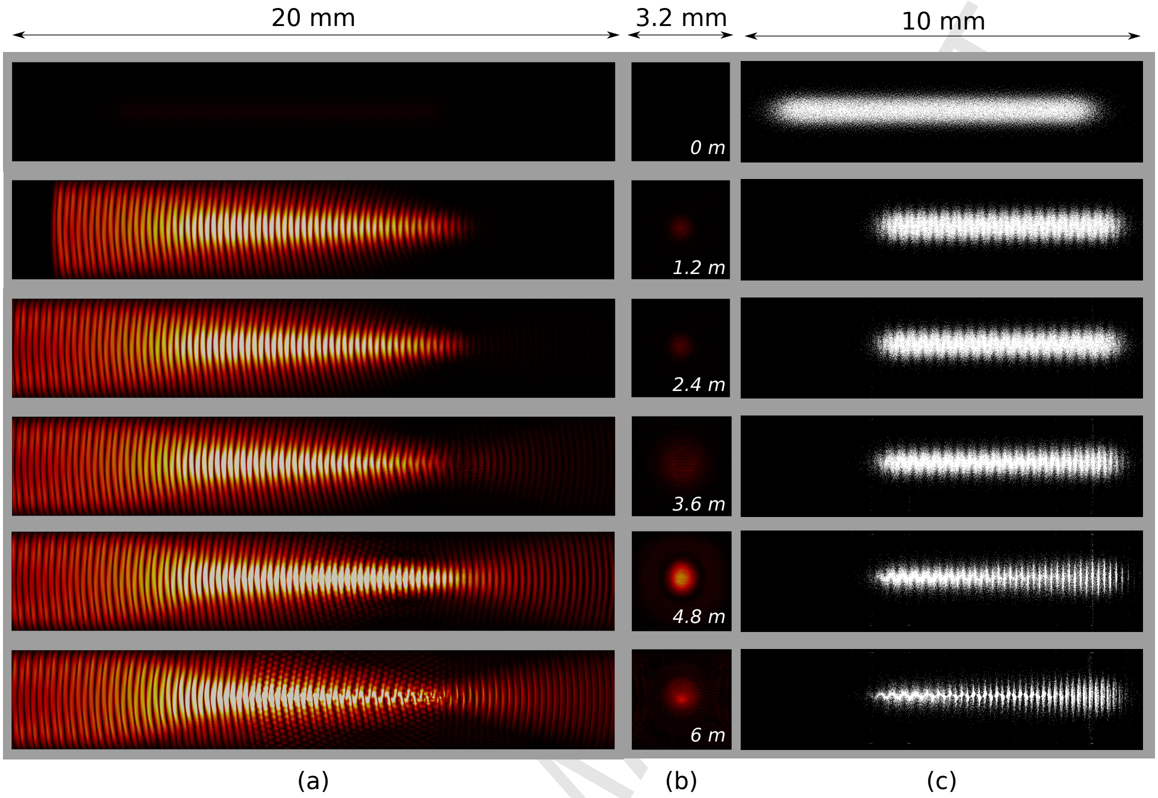

Figure 6: Snapshots of the radiated field profile taken at (a) $x = 0$ and (b) $z = 60\,\mu m$ plane and (c) the bunch profile viewed from the x axis.

regimes. To make sure that such effects are modeled correctly in MITHRA, we have performed comparisons with particle transport code ASTRA [46] for free-space propagation problem. Perfect agreement was observed between the two softwares, which are not presented here for the sake of brevity.

In Fig. 8a, we are comparing the solution of the FEL problem using MITHRA and Genesis 1.3 with and without considering the space-charge effect. As observed in the results, the effect of space-charge on the radiation gain predicted by MITHRA is much stronger than the same effect predicted by Genesis. This is attributed to the assumption of periodic variations in the space-charge force made in TDA algorithm. If such a hypothesis is correct, the observed discrepancy should reduce once the radiation from a longer bunch is simulated, because the accuracy of periodicity assumption increases for longer bunches. Indeed, this is observed after repeating the simulation for longer electron bunches with similar charge and current densities. The results of such a study is illustrated in Fig. 8b.

When space-charge effect is considered in a FEL simulation, equations (6) and (7) are solved in parallel using the charge and current excitations. It is important to examine if the Lorentz gauge is maintained in the calculated fields and no static field is built up in the computations. For this purpose, an error function is defined, which represents the relative amount of energy in the Lorentz gauge field with respect to the divergence of $\boldsymbol{A}$ field:

$$e_L = \frac{\int_V \|\nabla \cdot \boldsymbol{A} + \frac{1}{c^2}\frac{\partial \varphi}{\partial t}\|^2 dv}{\int_V \|\nabla \cdot \boldsymbol{A}\|^2 dv}, \tag{57}$$

where V stands for the total computational domain. Fig. 9a shows the temporal variations of the error function during the simulation for different number of macro-particles. The initial error starts from large values due to the entrance of macro-particles in the computational domain and also the fringing field section of the undulator. Note that the approximate fringing fields calculated according to (51) is not a divergence-less magnetic field. However, after complete entrance in the undulator and radiation, the error function relaxes down to small values. Furthermore, it is observed that the error in gauge condition is decreasing with number of macro-particles which is an evidence of no static field accumulation [34]. In Fig. 9b, the computed power for

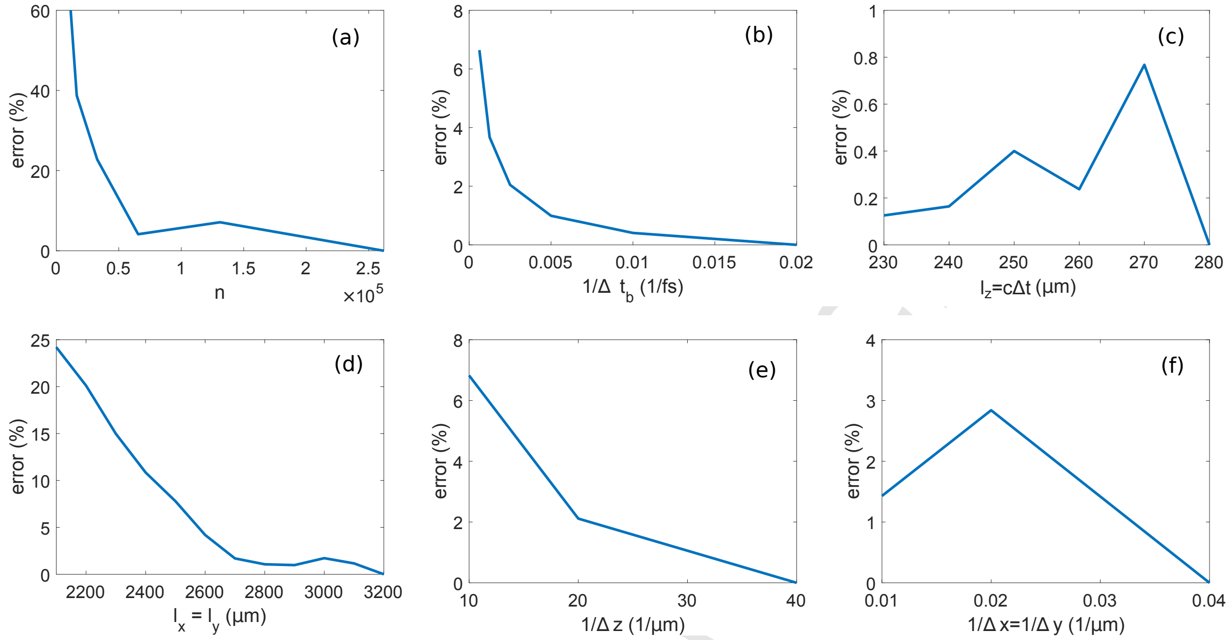

Figure 7: Convergence study for the different involved parameters in the considered FEL simulation: (a) n, (b) Δt_b, (c) l_z, (d) $l_x = l_y$, (e) Δz and (f) $\Delta x = \Delta y$

different number of macro-particles is depicted. This study shows that the error value is small enough to have negligible effect on the output results. We comment that this error calculation is performed within the main code and is not a capability offered by MITHRA to the users.

3.1.5. *Computation performance*

A potential user of the code is usually interested in the total computation resources required for a specific FEL simulation. To clarify such features, the study on the computation performance for MPI parallelized code is presented in Fig. 10, where the total computation time is depicted in terms of the number of processors. The simulation with 131072 macro-particles, a grid with 11’468’800 cells and 37’500 time steps is taken into account. The code is run on a E5-2698 v4 2.20 GHz machine with 80 CPUs, 20 Cores, and 512 GB Memory. It is observed that running on 40 CPUs is optimal for this problem. This number increases for larger and more demanding examples. In case of the run on 40 CPUs, field update on the computational grid, motion update of the bunch macro-particles and the computation of the total radiated field together with the required Fourier transform take 44%, 28%, and 28% of the total computational time, respectively. The reason for equal computation time for one and two processors lies behind the structure of the machine.

3.2. *Example 2: Seeded UV FEL*

3.2.1. *Problem Definition*

As the second example, we consider a seeded FEL in the UV regime to verify the implemented features for simulating a seeded FEL. The parameters of the considered case are taken from [10], which are tabulated in table 3.2.1. The bunch distribution is again assumed to be uniform with a long current profile (~1000 times the radiation wavelength) in order to compare the results with the steady state simulations. For the same reason, the seed pulse length is considered to be infinitely long, i.e. a continuous wave pulse. The transverse energy spread is calculated for a bunch with normalized transverse emittance equal to 0.97 mm mrad. Because of the very long bunch compared to the previous example, the number of required macro-particles to obtain convergent results is 8 times larger. Furthermore, the stronger undulator parameter dictates a smaller time step for the simulation of bunch dynamics. Note that MITHRA, takes the bunch step value as an initial guess, it automatically adjusts the value based on the calculated time step for mesh update.

3.2.2. *Simulation Results*

Fig. 11a shows the radiated power in terms of traveled undulator distance computed using MITHRA and Genesis. As observed again in this example, the results

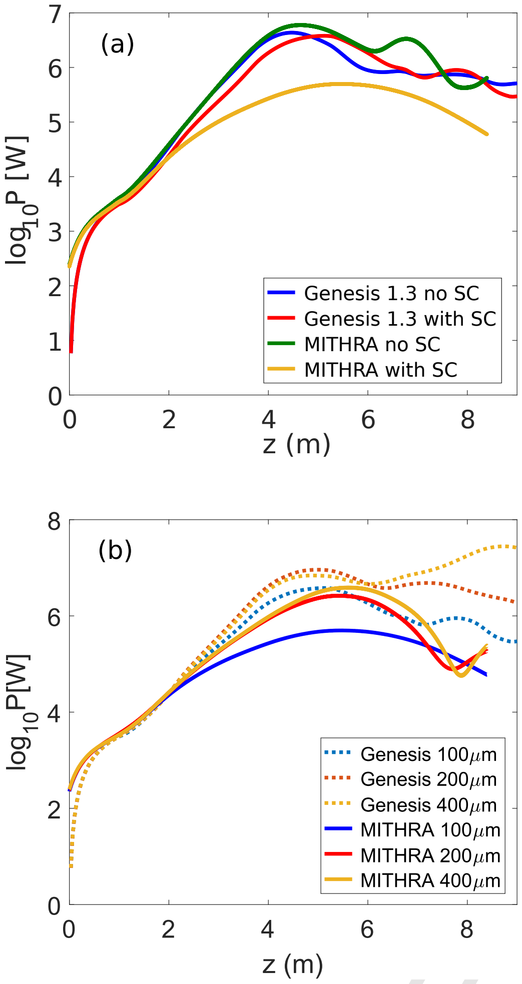

Figure 8: The total radiated power calculated at 110 μm distance from the bunch center in terms of the traveled undulator length (a) with and without space-charge consideration and (b) various lengths of the bunch with space-charge assumption.

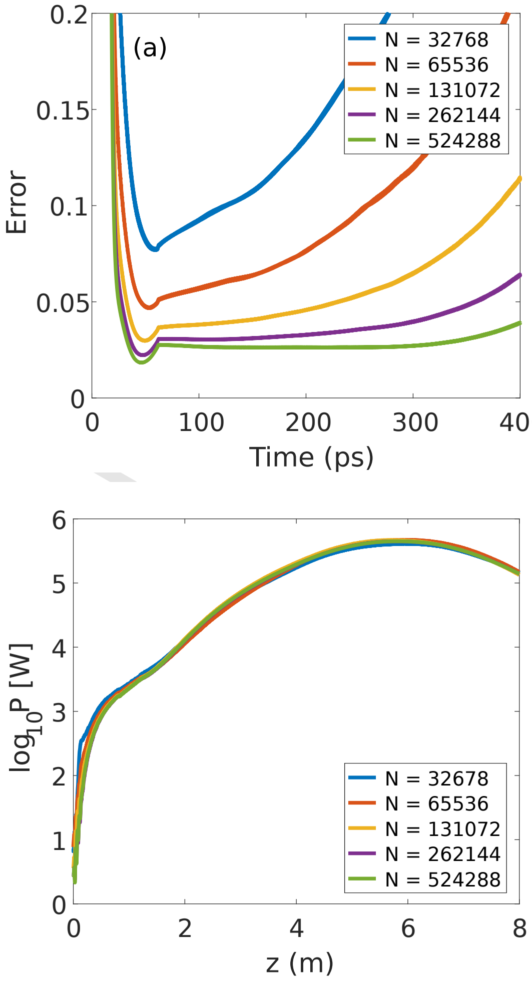

Figure 9: (a) Error in the gauge condition versus time is depicted for various number of macro-particles and (b) the total radiated power for the same number of macro-particles are shown.

agree very well in the seeded and gain regime, with notable discrepancies in the saturation regime. In Fig. 11b, the bunch profile after 12 m propagation in the undulator is also depicted. The micro-bunching of the large bunch is only visible once a zoom into a part of the bunch is considered. The investigation of the results with and without considering space-charge effect shows that in the seeded and gain intervals, space-charge plays a negligible role. However, in the saturation regime the effect of space-charge predicted by MITHRA is stronger than the effect predicted by Genesis.

3.3. *Example 3: Hard X-ray FEL*

3.3.1. *Problem Definition*

In the third example, simulation of a problem with parameter sets corresponding to the short pulse regime of the hard X-ray FEL source in the LCLS facility is pursued. The parameters considered in this example are tabulated in table 3.3.1.

3.3.2. *Simulation Results*

Fig. 12a shows the computed radiated power in terms of traveled undulator distance with and without consideration of space-charge effects. According to the 1D FEL theory, the FEL gain length for this example is around 0.92 m, which predicts saturation after around 18 m of undulator length. However, due to 3D effects

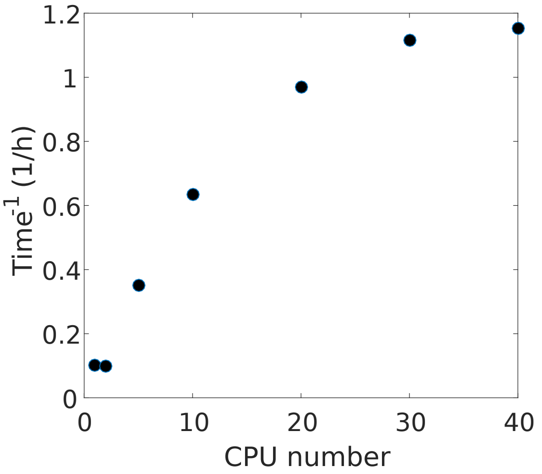

Figure 10: Reverse of total computation time versus the total number of processors.

this saturation length is slightly longer than the predictions of 1D FEL theory. Here, saturation length of about 22 m is observed for a space-charge free simulation. In addition, the space-charge effect seems to be considerable after 10 m of undulator propagation, which contradicts with the typical assumptions that such effects are negligible for multi-GeV beams. This large space-charge effect, not observed in the previous examples, is occurring due to the very short bunch length, which intensifies the Coulomb repulsion forces at the head and tail of the bunch. A rough estimate of the Coulomb field leads to 1 V/m electric field, which in 10 meters of free propagation adds a displacement about 8 nm to the relativistic electrons. This value being ten times larger than the radiation wavelength confirms the strong effect of space-charge forces. In the beginning of the radiation, some artifacts are observed for the calculation with space-charge effect. These artifacts are emerging because of the unrealistic modeling of fringing fields at the entrance of the undulator, which leads to nonzero magnetic field divergence. To correct for such effects, numerical distribution of the fringing fields should be taken into account. We comment that these results are merely simulating the interaction tabulated in table 3.3.1. In real FEL implementation, several focusing stations between undulator sections are realized to prevent the growth of the bunch size, thereby minimizing the space-charge effects in the FEL operation.

Table 3: Parameters of the UV seeded FEL configuration considered as the second example.

FEL parameter	Value
Current profile	Uniform
Bunch size	$(95.3 \times 95.3 \times 150)\,\mu$m
Bunch charge	54.9 pC
Bunch energy	200 MeV
Bunch current	110 A
Longitudinal momentum spread	0.01%
Normalized emittance	0.97 μm-rad
Undulator period	2.8 cm
Magnetic field	0.7 T
Undulator parameter	1.95
Undulator length	15 m
Radiation wavelength	0.265 μ m
Electron density	2.52×10^{14} 1/cm^3
Gain length (1D)	8.9 cm
FEL parameter	0.015
Cooperation length	3.34 μm
Initial bunching factor	0.0
Seed type	Gaussian beam
Seed focal point	70 cm
Seed beam radius	183.74 μm
Seed pulse length	infinite
Seed power	10 kW

3.4. Example 4: Optical Undulator

As explained in the introduction, one of the milestones considered for the development of MITHRA is full-wave simulation of inverse Compton scattering (ICS) or the so-called optical undulator. The possibility of lasing or the so-called micro-bunching in an electron beam due to an interaction with a counter-propagating laser beam has been under debate for several years. A full-wave analysis of such an interaction definitely gives valuable physical insight to this process. Note that the classical treatment of this interaction within MITHRA does not allow for consideration of quantum mechanical effects. It is known that the radiation of photons results in a backward force on electrons which leads to a change in their momenta. In the spontaneous radiation regime, the ratio $\rho_1 = \hbar\omega/\gamma mc^2$, representing the amount of quantum recoil due to each photon emission, quantifies this effect. In the FEL gain regime, $\rho_2 = (\hbar\omega/2\rho_{FEL}\gamma mc^2)^2$, with ρ_{FEL} being the FEL parameter, estimates the level of quantum recoil influence on the gain process [47, 48]. The use of classical formulation for optical undulators is only valid if $\rho_1 \ll 1$ and $\rho_2 \ll 1$.

Before embarking on the analysis and interpretation of results for a typical ICS experiment, a benchmark to validate the analysis of optical undulators using FDTD/PIC is presented. It is known that electron trajectories in a static undulator with undulator parameter

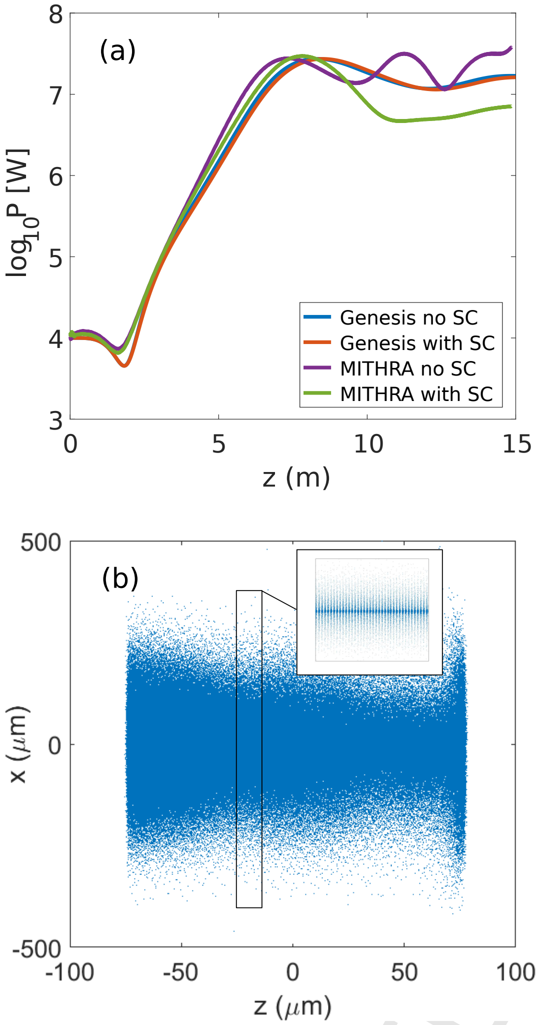

Figure 11: (a) The total radiated power measured at 80 μm distance from the bunch center in terms of the traveled undulator length and (b) the bunch profile at 12 m from the undulator begin.

K and periodicity λ_u are similar to the trajectories in an electromagnetic undulator setup with normalized vector potential $a_0 = K$ and wavelength $\lambda_l = 2\lambda_u$ [49]. We take the first SASE FEL example in table 3.1.1 into account and analyze the same configuration but with an equivalent optical undulator, namely a plane wave with normalized vector potential $a_0 = 1.417$, and wavelength $\lambda_u = 6$ cm. Fig. 13 illustrates a comparison between the radiated infrared light for the static and optical undulator cases. The very close agreement between the two results validates the implementation of optical undulators in MITHRA.

The parameters of the optical undulator setup, considered as the fourth example, are tabulated in table

Table 4: Parameters of the hard X-ray FEL configuration considered as the third example.

FEL parameter	Value
Current profile	Uniform
Bunch size	$(30.0 \times 30.0 \times 0.8)\,\mu$m
Bunch charge	20.0 pC
Bunch energy	6.7 GeV
Bunch current	7.5 kA
Longitudinal momentum spread	0.1%
Normalized emittance	0.2 μm-rad
Undulator period	3.0 cm
Undulator parameter	3.5
Undulator length	40 m
Radiation wavelength	0.62 nm
Gain length (1D)	0.92 m
FEL parameter	0.0015
Cooperation length	19.3 nm
Initial bunching factor	0.0033

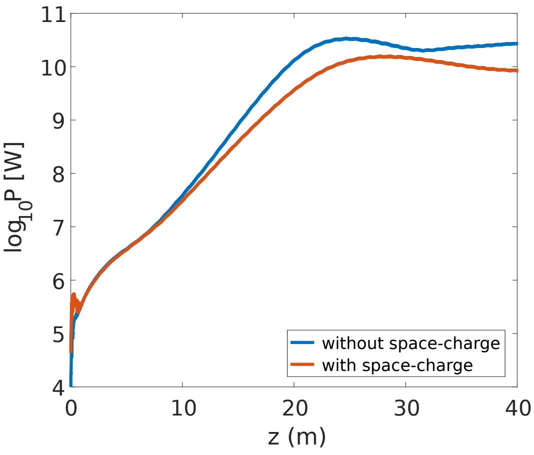

Figure 12: Total radiated power measured at 30 nm distance from the bunch center in terms of the traveled undulator length for the hard X-ray FEL source as the third example.

3.4. Since we observe deviations from the predictions of one-dimensional FEL theory in our simulations, we have not listed the parameters calculated using the 1D FEL theory. We believe the discrepancies are originated from the small number of electrons in each 3D wave bucket, i.e. only 2 electrons. This intensifies the 3D effects in the bunch interaction with counter-propagating laser pulse. We comment that for the listed parameters $\rho_1 = 2 \times 10^{-4}$ and $\rho_2 = 0.003$, which are much smaller than errors caused by space-time discretization.

Fig. 14a shows the radiated power in terms of travelled undulator distance detected 82 nm away from the bunch center. The effects of space-charge and energy spread (σ_E) of the bunch are illustrated through different comparisons. It is observed that the gain obtained in

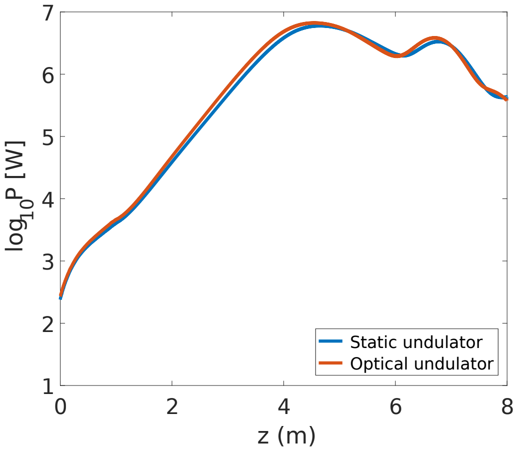

Figure 13: The total radiated power calculated at 110 μm distance from the bunch center in terms of the traveled undulator length compared for two cases of an optical and static undulator.

Table 5: Parameters of the FEL configuration with optical undulator considered as the third example.

FEL parameter	Value
Current profile	Uniform
Bunch size	$(60 \times 60 \times 144)$ nm
Bunch charge	0.45 fC
Bunch energy	15 MeV
Bunch current	0.93 A
Longitudinal momentum spread	0.1%
Normalized emittance	1.75 nm-rad
Laser wavelength	1 μm
Laser strength parameter	1.0
Pulse duration	4 ps
Laser pulse type	flat-top
Radiation wavelength	0.41 nm
Electron density	5.4×10^{18} 1/cm^3
Initial bunching factor	0.0

this regime is very small compared with a usual static undulators. The reason for this effect is the very large shot noise in the bunch because of the low number of particles in each micro-bunch. Note that in this simulation, each electron is modeled as one single particle without any initial modulation in the bunch distribution. The strong shot noise due to 3D effects causes a strong initial radiation, which reaches the expected saturation power after a low gain. The case with zero energy spread corresponds to initialization of the bunch particles with exactly the same momentum.

Another aspect in this regime of interaction is the generation of strong higher order harmonics, which are depicted up to the third harmonic in Fig. 14b. Note that the accuracy of the results decreases for higher harmonics due to the required resolution in the computational mesh. To show that the micro-bunching effect takes place in this regime as well, the bunching factor of the electron beam is depicted in Fig. 14c. The bunching of the electrons due to the ICS interaction is clearly observed in the plot of bunching factor. This increase in the bunching factor disappears when particle radiation is suppressed in the code. Therefore, one can conclude that despite the low-gain, micro-bunching takes place. This micro-bunching process is expected to increase the longitudinal coherence of the output radiation. However, due to very strong initial radiation and the noise caused by 3D effects no coherent amplification is observed. According to the depicted power and pulse shape, total number of emitted photons is approximately equal to 4.2×10^3.

To demonstrate the presented hypothesis related to the micro-bunching of bunches with low number of electrons per wavelength bucket, we perform an *unreal* simulation, where each electron is presented by 1000 particles. The thousand particles are distributed evenly throughout each wavelength bucket in order to drastically reduce the shot noise level. In this case, each particle represents a charge 1000 times smaller than the charge of one electron. In addition, we assume an initial bunching factor equal to 0.001 for the input bunch to trigger the stimulated gain. In Fig. 15, the radiation of such a charge configuration is depicted. The results reveal the radiation start from much lower powers, possibility of achieving the radiation gain and saturating in the same power level as above.

This behavior and the contrast with simulation based on real number of electrons are described as follows: According to the FEL theory, the radiation gain is obtained due to periodic arrangement of radiators. Usually this principle is described as the initial incoherent radiation being proportional to N, whereas the coherent radiation of the modulated beam being proportional to N^2. Now, the question is how this N value is defined. The world is three-dimensional and N should be the number of electrons in a 3D coherence volume. When this number is two, the FEL principle predicts that the gain should be only twofold. However, 1D FEL theory does not consider particles in the 3D coherence volume and takes particles in 1D coherence length into account. Therefore, modelling such a problem strongly affected by 3D effects suffers from inaccurate assumptions in 1D FEL theory. The visualization of the fields also shows strong oscillations which disagrees with slow-varying approximation considered in typical FEL codes. The reason why this gain is becoming large when the number of macro-particles is increased (Fig. 15) originates from the above effect. Indeed the number of radiators

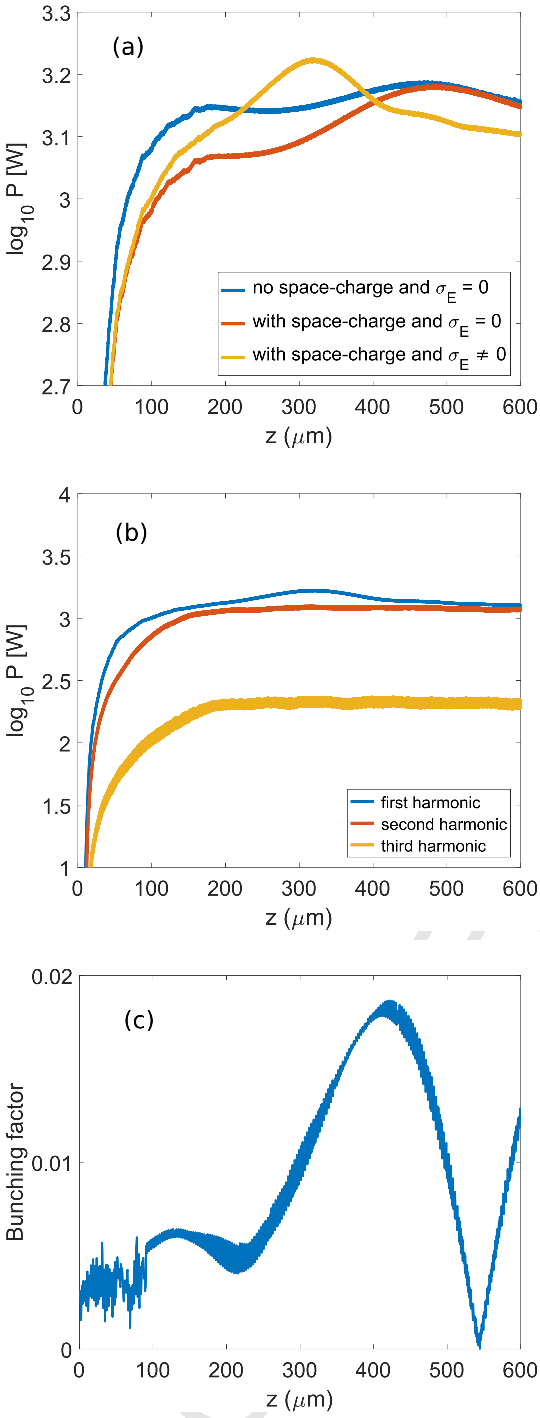

Figure 14: (a) The total radiated power measured at 82 nm distance from the bunch center in terms of the traveled distance, (b) the same radiation power for various harmonic orders, (c) mean bunching factor over the whole bunch during the ICS interaction.

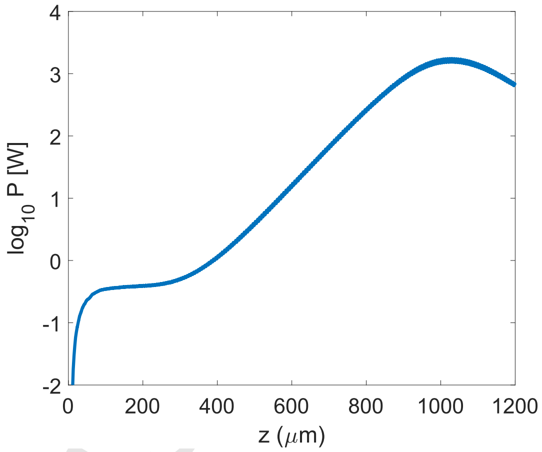

Figure 15: The total radiated power measured at 82 nm distance from the bunch center in terms of the traveled distance for an imaginary bunch where each electron is represented by a cloud of 1000 particles.

per coherence volume N is so large that the cumulative 3D effects are vanished. This results in a low initial noise and clear observation of the radiation gain. Consequently, the presented simulation by MITHRA agrees with the already developed FEL theory, according to which low number of electrons per coherence volume prevents achieving the radiation gain, even if the electron bunch is micro-bunched.

4. Conclusion

Using the FDTD algorithm to solve time domain Maxwell's equations combined with the PIC method to solve for the particle trajectories, software MITHRA is developed for the full-wave numerical modeling of a FEL process. The algorithm takes advantage of the drastically reduced computational costs when Lorentz transformations are employed to solve the problem in the bunch rest frame. The developed software provides a proper tool for accurate analysis of free electron lasers. In addition, novel schemes to develop new radiation sources can be tested using this tool. Several benchmarks were presented to show the reliability of the results, including an infra-red FEL and a UV SASE FEL. The agreement between the results obtained by MITHRA and the standard software Genesis 1.3 show the reliability of the results produced by both softwares. Furthermore, the software is utilized to simulate an inverse Compton scattering interaction including the effect of particle radiation on the bunch distribution. The feasibility of micro-bunching is observed although no radiation gain is achieved. This is believed to occur due to strong 3D effects in particle radiation which degrade the radiation gain.

5. Acknowledgement

This work was supported by the European Research Council under the European Unions Seventh Framework Programme (FP/2007-2013) / ERC Grant Agreement n. 609920, the Center for Free-Electron Laser Science at DESY and the excellence cluster The Hamburg Centre for Ultrafast Imaging - Structure, Dynamics and Control of Matter at the Atomic Scale of the Deutsche Forschungsgemeinschaft. A. Y. is acknowledging support by a George-Foster research fellowship from Alexander von Humboldt foundation. We are also thankful to Moein Fakhari for his help with benchmarking the space-charge implementation in MITHRA and comparison with ASTRA.

References

[1] P. Schmüser, M. Dohlus, J. Rossbach, Ultraviolet and soft X-ray free-electron lasers: introduction to physical principles, experimental results, technological challenges, Vol. 229, Springer, 2008.

[2] E. L. Saldin, E. E. A. Schneidmiller, M. V. Yurkov, The physics of free electron lasers, Springer, 2000.

[3] H. P. Freund, Principles of free-electron lasers, Springer Science & Business Media, 2012.

[4] E. Jaeschke, S. Khan, J. R. Schneider, J. B. Hastings, Synchrotron Light Sources and Free-Electron Lasers, Springer, 2015.

[5] S. Reiche, Genesis 1.3: a fully 3d time-dependent fel simulation code, Nuclear Instruments and Methods in Physics Research Section A: Accelerators, Spectrometers, Detectors and Associated Equipment 429 (1) (1999) 243–248.

[6] S. G. Biedron, H. P. Freund, S. V. Milton, 3d fel code for the simulation of a high-gain harmonic generation experiment, in: Optoelectronics' 99-Integrated Optoelectronic Devices, International Society for Optics and Photonics, 1999, pp. 96–108.

[7] T. M. Tran, J. Wurtele, TDA - a three-dimensional axisymmetric code for free-electron-laser (fel) simulation, Computer Physics Communications 54 (2) (1989) 263–272.

[8] B. Faatz, W. Fawley, P. Pierini, S. Reiche, G. Travish, D. Whittum, J. Wurtele, Tda3d: Updates and improvements to the widely used three-dimensional free electron laser simulation, Nuclear Instruments and Methods in Physics Research Section A: Accelerators, Spectrometers, Detectors and Associated Equipment 393 (1) (1997) 277–279.

[9] W. Fawley, A user manual for {GINGER} and itspost-processor {XPLOTGIN}, LBNL-49625Rev. 1.

[10] L. Giannessi, Overview of perseo, a system for simulating fel dynamics in mathcad, in: Proceedings of the Free-Electron Laser Conference, 2006, pp. 91–94.

[11] A. Bacci, C. Maroli, V. Petrillo, A. Rossi, L. Serafini, P. Tomassini, Compact x-ray free-electron laser based on an optical undulator, Nuclear Instruments and Methods in Physics Research Section A: Accelerators, Spectrometers, Detectors and Associated Equipment 587 (2) (2008) 388–397.

[12] R. J. Dejus, O. A. Shevchenko, N. A. Vinokurov, An integral equation based computer code for high-gain free-electron lasers, Nuclear Instruments and Methods in Physics Research Section A: Accelerators, Spectrometers, Detectors and Associated Equipment 429 (1) (1999) 225–228.

[13] E. Saldin, E. Schneidmiller, M. Yurkov, Fast: a three-dimensional time-dependent fel simulation code, Nuclear Instruments and Methods in Physics Research Section A: Accelerators, Spectrometers, Detectors and Associated Equipment 429 (1) (1999) 233–237.

[14] I. A. Andriyash, R. Lehe, V. Malka, A spectral unaveraged algorithm for free electron laser simulations, Journal of Computational Physics 282 (2015) 397–409.

[15] L. Campbell, B. McNeil, Puffin: A three dimensional, unaveraged free electron laser simulation code, Physics of Plasmas (1994-present) 19 (9) (2012) 093119.

[16] S. Biedron, Y. Chae, R. J. Dejus, B. Faatz, H. Freund, S. Milton, H.-D. Nuhn, S. Reiche, Multi-dimensional free-electron laser simulation codes: a comparison study, Nuclear Instruments and Methods in Physics Research Section A: Accelerators, Spectrometers, Detectors and Associated Equipment 445 (1) (2000) 110–115.

[17] S. Mangles, C. Murphy, Z. Najmudin, A. Thomas, J. Collier, A. Dangor, E. Divall, P. Foster, J. Gallacher, C. Hooker, et al., Monoenergetic beams of relativistic electrons from intense laser–plasma interactions, Nature 431 (7008) (2004) 535–538.

[18] J. Faure, Y. Glinec, A. Pukhov, S. Kiselev, S. Gordienko, E. Lefebvre, J.-P. Rousseau, F. Burgy, V. Malka, A laser–plasma accelerator producing monoenergetic electron beams, Nature 431 (7008) (2004) 541–544.

[19] C. Geddes, C. Toth, J. Van Tilborg, E. Esarey, C. Schroeder, D. Bruhwiler, C. Nieter, J. Cary, W. Leemans, High-quality electron beams from a laser wakefield accelerator using plasma-channel guiding, Nature 431 (7008) (2004) 538–541.

[20] T. Tajima, J. Dawson, Laser electron accelerator, Physical Review Letters 43 (4) (1979) 267.

[21] O. Lundh, J. Lim, C. Rechatin, L. Ammoura, A. Ben-Ismail, X. Davoine, G. Gallot, J.-P. Goddet, E. Lefebvre, V. Malka, et al., Few femtosecond, few kiloampere electron bunch produced by a laser-plasma accelerator, Nature Physics 7 (3) (2011) 219–222.

[22] R. J. England, R. J. Noble, K. Bane, D. H. Dowell, C.-K. Ng, J. E. Spencer, S. Tantawi, Z. Wu, R. L. Byer, E. Peralta, et al., Dielectric laser accelerators, Reviews of Modern Physics 86 (4) (2014) 1337.

[23] E. A. Nanni, W. R. Huang, K.-H. Hong, K. Ravi, A. Fallahi, G. Moriena, R. D. Miller, F. X. Kärtner, Terahertz-driven linear electron acceleration, Nature communications 6 (2015) 8486.

[24] A. Fallahi, M. Fakhari, A. Yahaghi, M. Arrieta, F. X. Kärtner, Short electron bunch generation using single-cycle ultrafast electron guns, Physical Review Accelerators and Beams 19 (8) (2016) 081302.

[25] F. Kärtner, F. Ahr, A.-L. Calendron, H. Çankaya, S. Carbajo, G. Chang, G. Cirmi, K. Dörner, U. Dorda, A. Fallahi, et al., Axsis: exploring the frontiers in attosecond x-ray science, imaging and spectroscopy, Nuclear Instruments and Methods in Physics Research Section A: Accelerators, Spectrometers, Detectors and Associated Equipment 829 (2016) 24–29.

[26] A. Taflove, S. C. Hagness, Computational electrodynamics, Artech house publishers, 2000.

[27] J.-L. Vay, Noninvariance of space- and time-scale ranges under a lorentz transformation and the implications for the study of relativistic interactions, Phys. Rev. Lett. 98 (2007) 130405.

[28] P. Sprangle, A. Drobot, Stimulated backscattering from rel-

ativistic unmagnetized electron beams, Journal of Applied Physics 50 (4) (1979) 2652–2661.

[29] P. Yu, X. Xu, V. K. Decyk, W. An, J. Vieira, F. S. Tsung, R. A. Fonseca, W. Lu, L. O. Silva, W. B. Mori, Modeling of laser wakefield acceleration in lorentz boosted frame using em-pic code with spectral solver, Journal of Computational Physics 266 (2014) 124–138.

[30] J.-L. Vay, I. Haber, B. B. Godfrey, A domain decomposition method for pseudo-spectral electromagnetic simulations of plasmas, Journal of Computational Physics 243 (2013) 260–268.

[31] J.-L. Vay, D. Grote, R. Cohen, A. Friedman, Novel methods in the particle-in-cell accelerator code-framework warp, Computational Science & Discovery 5 (1) (2012) 014019.

[32] W. Fawley, J.-L. Vay, Use of the lorentz-boosted frame transformation to simulate free-electron laser amplifier physics, in: AIP Conference Proceedings, Vol. 1086, AIP, 2009, pp. 346–350.

[33] I. Andriyash, E. dHumières, V. Tikhonchuk, P. Balcou, X-ray amplification from a raman free-electron laser, Physical review letters 109 (24) (2012) 244802.

[34] T. Umeda, Y. Omura, T. Tominaga, H. Matsumoto, A new charge conservation method in electromagnetic particle-in-cell simulations, Computer Physics Communications 156 (1) (2003) 73–85.

[35] K. L. Shlager, J. B. Schneider, Comparison of the dispersion properties of several low-dispersion finite-difference time-domain algorithms, IEEE Transactions on Antennas and Propagation 51 (3) (2003) 642–653.

[36] B. Finkelstein, R. Kastner, Finite difference time domain dispersion reduction schemes, Journal of Computational Physics 221 (1) (2007) 422–438.

[37] J. P. Boris, Acceleration calculation from a scalar potential., Tech. rep., Princeton Univ., NJ Plasma Physics Lab. (1970).

[38] J. Boris, Relativistic plasma simulation-optimization of a hybrid code, in: Proc. Fourth Conf. Num. Sim. Plasmas, Naval Res. Lab, Wash. DC, 1970, pp. 3–67.

[39] J. D. Jackson, R. F. Fox, Classical electrodynamics, American Journal of Physics 67 (1999) 841.

[40] D. Sagan, J. Crittenden, D. Rubin, E. Forest, A magnetic field model for wigglers and undulators, in: Particle Accelerator Conference, 2003. PAC 2003. Proceedings of the, Vol. 2, IEEE, 2003, pp. 1023–1025.

[41] C. Pellegrini, A. Marinelli, S. Reiche, The physics of x-ray free-electron lasers, Reviews of Modern Physics 88 (1) (2016) 015006.

[42] S. Reiche, Numerical studies for a single pass high gain free-electron laser, Tech. rep., DESY (2000).

[43] C. Penman, B. McNeil, Simulation of input electron noise in the free-electron laser, Optics Communications 90 (1) (1992) 82 – 84.

[44] C. Maroli, V. Petrillo, Effects of the low-frequency backward wave in high-gain free-electron lasers, Optics communications 183 (1) (2000) 139–147.

[45] T.-M. Tran, J. Wurtele, Review of free-electron-laser (fel) simulation techniques, Tech. rep. (1990).

[46] K. Flöttmann, et al., Astra: A space charge tracking algorithm, Manual, Version 3 (2011) 2014.

[47] R. Bonifacio, N. Piovella, G. Robb, A. Schiavi, Quantum regime of free electron lasers starting from noise, Physical Review Special Topics-Accelerators and Beams 9 (9) (2006) 090701.

[48] R. Bonifacio, N. Piovella, G. Robb, Quantum theory of sase fel, Nuclear Instruments and Methods in Physics Research Section A: Accelerators, Spectrometers, Detectors and Associated Equipment 543 (2) (2005) 645–652.

[49] E. Esarey, S. K. Ride, P. Sprangle, Nonlinear thomson scattering of intense laser pulses from beams and plasmas, Physical Review E 48 (4) (1993) 3003.